Linear stability of thermocapillary flow in a droplet attached to a hot or cold substrate

Lukas Babor* and Hendrik C. Kuhlmann
Institute of Fluid Mechanics and Heat Transfer, TU Wien, Getreidemarkt 9, 1060 Wien, Austria

(Received 26 April 2023; accepted 18 October 2023; published 27 November 2023)

The symmetry-breaking instability of the steady axisymmetric thermocapillary flow in a nonvolatile sessile droplet on a hot or cold substrate under zero gravity conditions is investigated by linear stability analysis. The dependence of the critical Marangoni number on the contact angle and the Prandtl number is computed, and the structures of the most dangerous perturbation modes are analyzed. For a small contact angle and a high-Prandtl-number droplet with $\mathrm{Pr} = 16.36$ (corresponding to 1 cSt silicone oil) on a hot wall, we find classical Marangoni instabilities near the center of the droplet. In contrast, no instability is observed for small-contact-angle droplets on a cold wall. For large contact angles with $\alpha > 90^\circ$ either on a hot or a cold wall, the first instability of the basic axisymmetric toroidal vortex is inertial for low Prandtl numbers and of hydrothermal-wave type for high Prandtl numbers.

DOI: 10.1103/PhysRevFluids.8.114003

I. INTRODUCTION

Thermocapillary convection in sessile droplets has many applications. These range from art [1] to soldering [2], forensic science [3,4], epidemiological risk assessment [5], inkjet [6,7] and microelectronic [8,9] printing, and medical diagnostics [10–13]. Related to many of these fields, the nonuniform deposition of suspended particles during evaporation, known as *coffee-stain effect* [14,15], is of fundamental interest. The physics behind the coffee-stain effect has been recently reviewed by Wilson and D'Ambrosio [16], while Zang *et al.* [17] provide a comprehensive review of its applications.

The flow in sessile droplets is mainly driven by temperature gradients which can arise due to the latent heat release during evaporation, or if the substrate and the ambient atmosphere are at different temperatures. For weak flow and a perfect axisymmetric geometry, the flow is also axisymmetric. However, if the driving force is sufficiently strong, then symmetry-breaking hydrodynamic instabilities may lead to three-dimensional flow. These include Marangoni instabilities caused by a temperature gradient perpendicular to the interface [18] and thermocapillary instabilities when the temperature varies mainly tangentially to the interface, like hydrothermal waves [19] or radial convection rolls [20–22]. For large droplets, buoyancy forces may also play a role [23–25]. A recently discovered interesting phenomenon in thermocapillary-driven flow in droplets is the clustering of small particles in form of dynamic particle accumulation structures when the flow arises as a hydrothermal wave [26].

The present investigation is concerned with the flow instabilities in sessile thermocapillary liquid droplets when the ambient temperature differs from the wall temperature. The heat transfer to or from droplets involves temperature gradients that have both a normal and a tangential component. The individual instability mechanisms which are potentially relevant for sessile droplets are best explained for plane layers when only one of the components of the temperature gradient is present.

*Corresponding author: lukas.babor@tuwien.ac.at

In the classical Marangoni instability [18] of a quiescent liquid layer bounded by a wall and a free surface, the temperature gradient is perpendicular to the interface. In this case, a local perturbation of the free-surface temperature creates a tangential surface flow which, by continuity, involves an advection of temperature normal to the interface. When ∇T is perpendicular and directed into the liquid phase (if the liquid is cooled from the gas phase) there exists a critical temperature gradient when advection dominates diffusion, such that the surface temperature perturbation is amplified. Otherwise, it is damped. The critical perturbations arise as steady convection rolls which organize themselves by nonlinear mechanism and/or geometric constraints into regular flow patterns. In the case of hexagonal or square cells in a liquid layer, the perturbation flow at the center of a cell is directed towards the free surface [27]. If buoyancy assists the mechanism (heating from below), then the instability is also called Bénard-Marangoni instability.

Contrary to the classical Marangoni instability of a quiescent liquid layer, a temperature gradient tangent to the free surface always causes a flow. In plane layers, the resulting plane shear flows can become unstable to hydrothermal waves [19,28] which propagate at a certain angle with respect to the direction of the temperature gradient, depending on the Prandtl number of the liquid. These waves can be inertial for small Prandtl numbers, or thermal for high Prandtl numbers. High-Prandtl-number hydrothermal waves also arise in thermocapillary liquid bridges [29] or cavities [30] and annular liquid pools [[31–33], and others]. They are characterized by strong internal perturbation temperature extrema which are amplified by a relatively weak thermocapillary perturbation flow acting on the internal basic-state temperature gradients.

When the temperature gradient on the free surface is oblique, but dominated by the normal component, the horizontal flow induced by the tangential part can advect the cellular patterns induced by the dominant normal part of the temperature gradient (Marangoni cells). The cells are typically transported from hot to cold surface regions, leading to traveling (Bénard-)Marangoni cells [34]. Zhu and Shi [22] emphasized that these traveling Marangoni cells must not be confused with hydrothermal waves, which travel in the opposite direction from cold to hot surface regions for high Prandtl numbers.

Bénard-Marangoni cells are typically observed near the center of a droplet [35] or near the contact line of a shallow droplet [22]. In both cases, the primary component of the temperature gradient and the acceleration of gravity are perpendicular to the interface. When the dominant component of the temperature gradient is parallel to the interface, it can drive a significant steady axisymmetric flow in droplets [25]. Associated with this are internal temperature gradients on which hydrothermal waves can grow by a coupling of strong internal temperature perturbations to weak ones on the free surface by a weak perturbation flow. Hydrothermal waves can be expected in droplets with larger contact angles [36]. The influence of buoyancy on the axisymmetric transport has been investigated by Masoudi and Kuhlmann [25] for single-component fluids and by Refs. [23], [24], and [37] for binary droplets.

Flow instabilities in nonisothermal liquid droplets are strongly affected by the confinement of the system, the shape of the interface, and evaporation. While evaporating droplets have been studied by several authors [e.g., Refs. [22,38,39]], only a few investigations considered the flow in nonvolatile droplets driven by the temperature difference between the substrate and the ambient gas [35,36] which is the subject of this work.

The instability of the flow in nonisothermal liquid droplets is governed by many parameters, the main ones being the thermocapillary Reynolds number, the contact angle, the Prandtl number, the Biot number, the Grashof number, and the Bond number. Therefore, a full characterization of the instabilities is still lacking. In the present investigation, we aim at a systematic investigation of the influence of the contact angle and the Prandtl number on the symmetry-breaking instabilities of the flow in nonisothermal droplets. These instabilities are expected to arise at a critical temperature difference between the wall and the ambiance, corresponding to a critical thermocapillary Reynolds number. To that end, a linear stability analysis is carried out of the steady axisymmetric flow in nonvolatile droplets adhering to a heated or cooled wall. To make possible a quasi-continuous

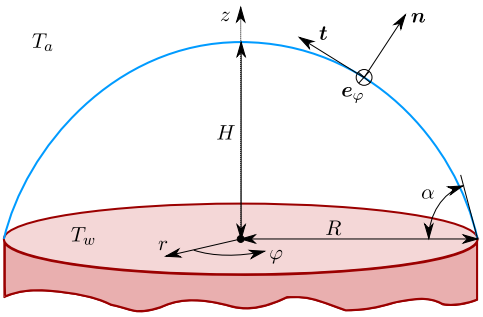

FIG. 1. Sketch of a sessile droplet with a spherical free surface (blue), radius R, and height H. The origin of the cylindrical coordinate system (r, φ, z) is located at the center of the droplet base (red). The surface normal and tangent vectors are $\boldsymbol{n}, \boldsymbol{t}$, and $\boldsymbol{e}_\varphi$.

parameter variation we consider zero gravity conditions and a uniform heat transfer coefficient along the free surface.

II. PROBLEM FORMULATION

We consider a droplet of a nonvolatile incompressible Newtonian liquid with density ρ, kinematic viscosity ν, thermal conductivity k, thermal diffusivity κ, and thermal expansion coefficient $\beta = -\rho^{-1}\partial_T \rho$. The droplet is adhering to the plane end surface of a cylindrical support of radius R such that the contact line is fixed by the sharp circular edge of the support rod. Under zero gravity conditions and in the absence of temperature gradients the equilibrium shape of the interface is a spherical cap of base-to-apex height H, depending on the contact angle α (Fig. 1).

A wall temperature T_w of a perfectly conducting substrate which differs from the ambient temperature with a uniform far-field $T_a \neq T_w$ leads to a nonuniform temperature distribution on the liquid-gas interface. Approximating the temperature dependence of the surface tension to linear order by $\sigma(T) = \sigma_0 - \gamma(T - T_0)$, where T_0 is the reference temperature, σ_0 the reference surface tension and $\gamma > 0$ the thermal surface tension coefficient, an interfacial flow is driven by the thermocapillary effect [40]. Here we select the reference temperature $T_0 = T_a$ and define the temperature difference $\Delta T = |T_w - T_a|$.

A. Governing equations

Several approximations are made to simplify the numerical analysis such that parametric studies become feasible. To that end, we consider small droplets such that buoyancy forces, quantified by the dynamic Bond number

$$\mathrm{Bd} = \frac{\rho g \beta H^2}{\gamma}, \tag{1}$$

where g is the acceleration of gravity, can be neglected. The influence of weak buoyancy will be considered, however, for a single representative case within the framework of the Boussinesq approximation. Furthermore, we take the limit of dominating mean surface tension σ_0 in which the Capillary number $\mathrm{Ca} = \gamma \Delta T/\sigma_0 \to 0$ and the static Bond number $\mathrm{Bo} = \rho g H^2/\sigma_0 \to 0$ vanish. In this limit, the shape of the interface is not affected by the flow and remains spherical. Its shape is only characterized by the aspect ratio

$$\Gamma = \frac{H}{R} = \tan(\alpha - \pi/2) + \frac{1}{\cos(\alpha - \pi/2)}, \tag{2}$$

which can also be expressed by the contact angle α. To model the heat transfer across the free surface we employ Newton's law of heat transfer in which the heat transfer coefficient h is assumed constant [for the spatial variation of the heat flux when the ambient atmosphere is taken into account, see, e.g., Refs. [41,42]] and in which the radiative heat transfer is neglected. The effect of radiation is considered in Appendix A. Owing to the low dynamic viscosity of gases at atmospheric pressure the viscous shear stress from the gas acting on the free surface is neglected as well. Except for the surface tension, all other thermophysical properties are assumed constant. The production and consumption of heat by mechanical work are neglected, as well as the effect of the internal energy of the free surface on the interfacial heat transfer [43].

Under the above approximations the flow is governed by the nondimensional incompressible Navier-Stokes equations

$$(\partial_t + \boldsymbol{u}\cdot\nabla)\boldsymbol{u} = -\nabla p + \nabla^2\boldsymbol{u} + \frac{\mathrm{Bd}\,\mathrm{Re}}{\Gamma^2}\theta\boldsymbol{e}_z, \tag{3a}$$

$$\nabla\cdot\boldsymbol{u} = 0, \tag{3b}$$

and the energy equation

$$(\partial_t + \boldsymbol{u}\cdot\nabla)\theta = \frac{1}{\mathrm{Pr}}\nabla^2\theta, \tag{3c}$$

where $\mathrm{Pr} = \nu/\kappa$ is the Prandtl number and $\mathrm{Bd} > 0$ ($\mathrm{Bd} < 0$) corresponds to a sessile (pendant) droplet of a fluid with $\beta > 0$. In Eq. (3) the length $\boldsymbol{x}$, velocity $\boldsymbol{u}$, pressure p and time t have been made dimensionless using viscous scales R, ν/R, $\rho(\nu/R)^2$ and R^2/ν, respectively. The reduced temperature $\theta = (T - T_a)/\Delta T$ ranges in $\theta \in [0, 1]$ in case of a hot wall and in $\theta \in [-1, 0]$ for a cold wall.

Using polar coordinates (r, φ, z) centered on the wall, and $\boldsymbol{u} = u\boldsymbol{e}_r + v\boldsymbol{e}_\varphi + w\boldsymbol{e}_z$, the no-slip and constant temperature boundary conditions on the wall at $z = 0$ and the uniqueness condition on the axis $r = 0$ require

$$\boldsymbol{u} = \theta \mp 1 = 0 \quad \text{on } z = 0, \tag{4a}$$

$$\partial_\varphi\boldsymbol{u} = \partial_\varphi p = \partial_\varphi\theta = 0 \quad \text{on } r = 0, \tag{4b}$$

where the $\mp$ sign indicates the wall being kept either hot or cold. On the spherical liquid-gas interface, denoted Γ_s, no-penetration and thermocapillary stress conditions are imposed

$$\boldsymbol{n}\cdot\boldsymbol{u} = 0 \quad \text{on } \Gamma_s, \tag{4c}$$

$$\boldsymbol{t}\cdot\mathsf{S}\cdot\boldsymbol{n} = -\mathrm{Re}\,\boldsymbol{t}\cdot\nabla\theta \quad \text{on } \Gamma_s, \tag{4d}$$

$$\boldsymbol{e}_\varphi\cdot\mathsf{S}\cdot\boldsymbol{n} = -\mathrm{Re}\,\boldsymbol{e}_\varphi\cdot\nabla\theta \quad \text{on } \Gamma_s, \tag{4e}$$

where $\mathsf{S} = [\nabla\boldsymbol{u} + (\nabla\boldsymbol{u})^{\mathrm{T}}]$ is the nondimensional viscous stress tensor, $\boldsymbol{e}_\varphi$ the azimuthal unit vector, $\boldsymbol{n}$ the outward unit vector normal to the interface, and $\boldsymbol{t}$ the tangential unit vector in a plane $\varphi =$ const. as sketched in Fig. 1. The thermocapillary Reynolds number is defined as

$$\mathrm{Re} = \frac{\gamma\Delta T R}{\rho\nu^2}. \tag{4f}$$

Finally, the heat transfer across the liquid-gas interface is modeled by Newton's law of cooling

$$\boldsymbol{n}\cdot\nabla\theta = -\mathrm{Bi}\,\theta \quad \text{on } \Gamma_s, \tag{4g}$$

in which the Biot number $\mathrm{Bi} = (h_c R)/k$ is defined using an effective constant (lump) heat transfer coefficient h_c. To reduce the parameter space we consider only two physically realistic values of the Biot number, $\mathrm{Bi} = 0.236$ and 0.4. With the Biot number kept constant the solution to Eq. (3) depends on the thermocapillary Reynolds number Re, the Prandtl number Pr, and the contact angle α. Instead of the Reynolds number, the Marangoni number $\mathrm{Ma} = \mathrm{RePr}$ may be employed as a control parameter when $\mathrm{Pr} \neq 0$.

To allow a comparison of the results obtained for shallow droplets with those for plane layers it is useful to define an alternative Marangoni number. In an infinitely extended plane layer, the basic flow is quiescent and conductive. In this case, the free-surface temperature is [44]

$$T_s = \frac{T_w + \mathrm{Bi}_H T_a}{1 + \mathrm{Bi}_H}, \tag{5}$$

where the Biot number $\mathrm{Bi}_H = h_c H/\lambda$ is based on the thickness H of the layer. For shallow droplets with a small aspect ratio $\Gamma \ll 1$ the apex temperature can be approximated by $T_{\mathrm{apex}} \approx T_s$ with $\mathrm{Bi}_H = \mathrm{Bi}\Gamma$. The temperature difference between the apex and the wall in a purely conducting shallow droplet can thus be approximated by

$$\Delta T_H = |T_w - T_{\mathrm{apex}}| \approx \frac{\mathrm{Bi}_H}{1 + \mathrm{Bi}_H}|T_w - T_a| = \frac{\mathrm{Bi}\,\Gamma}{1 + \mathrm{Bi}\,\Gamma}\Delta T. \tag{6}$$

This leads to the alternative Marangoni number, as for plane layers of depth H,

$$\mathrm{Ma}_H := \frac{\gamma \Delta T_H H}{\rho \nu \kappa} = \frac{\mathrm{Bi}\,\Gamma^2}{1 + \mathrm{Bi}\,\Gamma}\mathrm{Ma}, \tag{7}$$

suitable for shallow droplets. We shall use Ma_H as the control parameter, because the stability boundary in terms of Ma_H is less sensitive with respect to variations of Bi than the stability boundary in terms of Ma, even for large contact angles.

B. Linear stability analysis

Since the problem is invariant with respect to translations in t and φ, it admits a steady axisymmetric basic flow $(\boldsymbol{u}_0, \theta_0)(r, z)$ with $\boldsymbol{u}_0 = u_0 \boldsymbol{e}_r + w_0 \boldsymbol{e}_z$ and $v = \partial_\varphi = \partial_t = 0$ satisfying the symmetry conditions

$$u_0 = \partial_r w_0 = \partial_r p_0 = \partial_r \theta_0 = 0 \quad \text{on } r = 0. \tag{8}$$

The linear stability of the basic flow is investigated by linearizing (3) with respect to small perturbations $(\boldsymbol{u}', \theta')(r, \varphi, z, t)$ leading to

$$(\partial_t + \boldsymbol{u}_0 \cdot \boldsymbol{\nabla})\boldsymbol{u}' + (\boldsymbol{u}' \cdot \boldsymbol{\nabla})\boldsymbol{u}_0 = -\boldsymbol{\nabla} p' + \nabla^2 \boldsymbol{u}' + \frac{\mathrm{Bd}\,\mathrm{Re}}{\Gamma^2}\theta' \boldsymbol{e}_z, \tag{9a}$$

$$\boldsymbol{\nabla} \cdot \boldsymbol{u}' = 0, \tag{9b}$$

$$(\partial_t + \boldsymbol{u}_0 \cdot \boldsymbol{\nabla})\theta' + (\boldsymbol{u}' \cdot \boldsymbol{\nabla})\theta_0 = \frac{1}{\mathrm{Pr}}\nabla^2 \theta'. \tag{9c}$$

These equations are subject to formally the same boundary conditions as in Eq. (4), except that the temperature perturbation must vanish on the wall, i.e.,

$$\theta' = 0 \quad \text{at } z = 0. \tag{10}$$

Solutions to Eq. (9) are sought in the form of normal modes

$$\begin{pmatrix} \boldsymbol{u}' \\ p' \\ \theta' \end{pmatrix} = \begin{pmatrix} \hat{\boldsymbol{u}} \\ \hat{p} \\ \hat{\theta} \end{pmatrix}(r, z)\mathrm{e}^{\mu t + \mathrm{i}m\varphi} + \text{c.c.}, \tag{11}$$

where the complex growth rate $\mu = \varsigma + \mathrm{i}\omega$ consists of the real growth rate $\varsigma = \Re(\mu)$ and an oscillation frequency $\omega = \Im(\mu)$, m is the azimuthal wave number and c.c. denotes the complex conjugate. Inserting this Ansatz into Eq. (9) leads to a linear system of partial differential equations

$$\mu \begin{pmatrix} 1 & 0 & 0 \\ 0 & 0 & 0 \\ 0 & 0 & 1 \end{pmatrix} \begin{pmatrix} \hat{\boldsymbol{u}} \\ \hat{p} \\ \hat{\theta} \end{pmatrix} = \mathcal{L} \begin{pmatrix} \hat{\boldsymbol{u}} \\ \hat{p} \\ \hat{\theta} \end{pmatrix}, \tag{12}$$

where $\mathcal{L}$ is a linear differential operator with respect to r and z. The boundary conditions on the axis $r = 0$ for the amplitudes $\hat{\boldsymbol{u}}$, $\hat{p}$ and $\hat{\theta}$ depend on the azimuthal wave number m as follows:

$$m = 0 : \hat{u} = \hat{v} = \partial_r \hat{w} = \partial_r \hat{p} = \partial_r \hat{\theta} = 0 \quad \text{on } r = 0, \tag{13a}$$

$$m = 1 : \partial_r \hat{u} = \partial_r \hat{v} = \hat{w} = \hat{p} = \hat{\theta} = 0 \quad \text{on } r = 0, \tag{13b}$$

$$m > 1 : \hat{u} = \hat{v} = \hat{w} = \hat{p} = \hat{\theta} = 0 \quad \text{on } r = 0. \tag{13c}$$

They are obtained by inserting the Ansatz (11) into the equivalent of Eq. (4b) for the perturbation flow and using the continuity Eq. (9b). Discretization of Eq. (12) in r and z provides, together with the boundary conditions, a generalized eigenvalue problem

$$\mu \mathsf{M} \cdot \hat{\boldsymbol{x}} = \mathsf{A} \cdot \hat{\boldsymbol{x}}, \tag{14}$$

where the matrix A is the discrete approximation of $\mathcal{L}$, M is diagonal as in Eq. (12) and the eigenvector $\hat{\boldsymbol{x}}$ contains the nodal values or interpolation coefficients (depending on the discretization) of $\hat{\boldsymbol{u}}$, $\hat{p}$ and $\hat{\theta}$.

To find the linear stability boundary, characterized by a critical Reynolds (Re_c) or Marangoni number ($\mathrm{Ma}_{H,c}$), the eigenvalue problem is solved, and the lowest Reynolds number is determined such that the maximum real growth rate among all eigenvalues vanishes, i.e., $\max \varsigma = 0$.

III. NUMERICAL METHODS

A. Solution technique

The numerical solution follows the method of des Boscs and Kuhlmann [45] which is extended to cylindrical coordinates and a curved free surface. The governing equations for the basic state $(\boldsymbol{u}_0, \theta_0)$ and for the normal modes $(\hat{\boldsymbol{u}}, \hat{\theta})$ are discretized in the (r, z) plane by a continuous Galerkin finite-element method on a grid of triangular Taylor-Hood elements, where the velocity and temperature are approximated by quadratic, and the pressure by linear element-wise polynomial interpolation of the nodal values. The no-penetration condition at the free surface is enforced with the method of Nitsche [46], as described in Appendix B. Terms proportional to $1/r^2$ which do not vanish on the axis $r = 0$ for normal modes with the azimuthal wave number $m = 1$ are replaced using the incompressibility constraint (9b) to avoid the nonintegrable singularity. The approach of Gelfgat, Bar-Joseph and Yarin [47] is extended to the stress formulation of the Stokes subsystem, as explained in Appendix C.

The open-source finite-element solver FEniCS [48] is employed for the meshing in the (r, z) plane using an unstructured grid and for the discretization of weak forms. Given the number N of elements of the basic (unrefined) mesh in the radial direction, the contour of the curved free surface is approximated by $M = N^2/4$ line segments of uniform length per $\pi/2$ radians. The size of elements decreases towards the free surface, since the sides of the elements on the free surface coincide with the very short line segments representing the free surface. Except for the neighborhood of the free surface, the size of the elements is uniform in the basic mesh returned by the mesher. The elements of the basic mesh near the wall are then divided into halves. In the case of a cold substrate, thin boundary layers arise near the cold corner $(r, z) = (1, 0)$. Therefore, the elements within the distance of 0.04 and 0.01 from the contact line $(r, z) = (1, 0)$ are gradually refined up to $1/8$ and $1/64$ of the basic area of unrefined elements in the bulk for $\mathrm{Pr} < 1$ and $\mathrm{Pr} \geqslant 1$, respectively. A coarse mesh with $N = 20$ is shown in Fig. 2. The case of a hot wall does not require a corner refinement. However, for the hot wall, $m = 1$ and $\mathrm{Pr} \geqslant 1$, the elements adjacent to the axis $r = 0$ are split into halves and those near the apex $(r, z) = (0, \Gamma)$ are refined in the same way as the elements near the contact line in case of a cold wall.

The resulting nonlinear system of algebraic equations for the discrete basic state is solved using the Newton-Raphson method implemented in FEniCS. The discretization with the second-order Taylor-Hood elements leads to a quadratic convergence with N. The convergence is shown in Fig. 3 by monitoring the extremum of the Stokes stream function $\|\psi^{\mathrm{St}}\|_\infty$ of the basic flow as a function

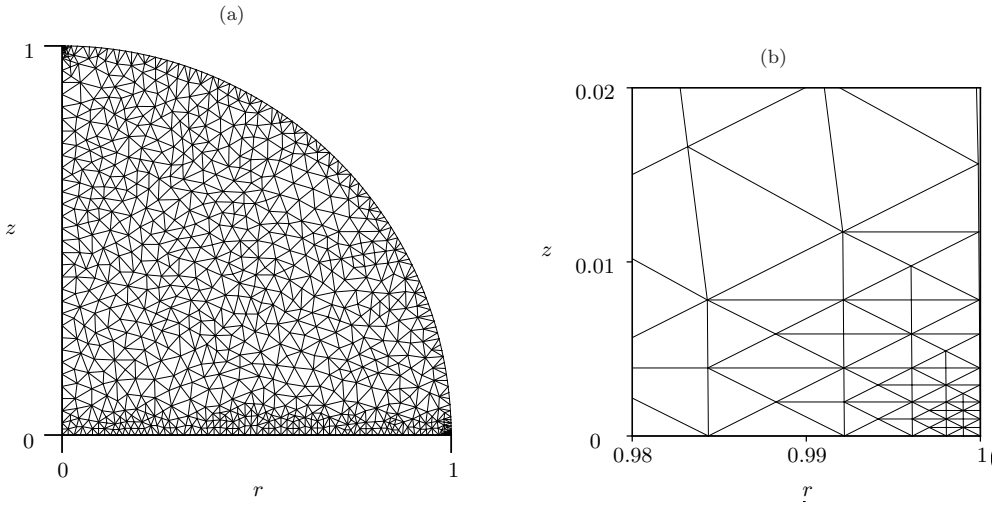

FIG. 2. (a) Example for a coarse mesh with $N = 20$ for $\alpha = 90^\circ$ suitable for a cold wall. (b) Zoom into the three-phase contact point.

of the mean number of cells per space direction $n = \sqrt{N \times \Gamma N}$. The convergence is not monotonic, because the unstructured grid changes with the resolution used.

Having computed the basic flow, the matrices A and M of the linear stability eigenproblem (14) are assembled in FEniCS on the same grid as used for the basic state and exported to SciPy. The eigenproblem is solved with `scipy.sparse.linalg.eigs` [49] which is an interface to the Arnoldi package [50]. Following the recommendation of des Boscs and Kuhlmann [45] we set the number of computed eigenvalues to 50, and the dimension of the Krylov space (parameter `ncv`) to 300. A shift-invert transformation [see chap. 3.2 of Ref. [50]] is necessary to find eigenvalues

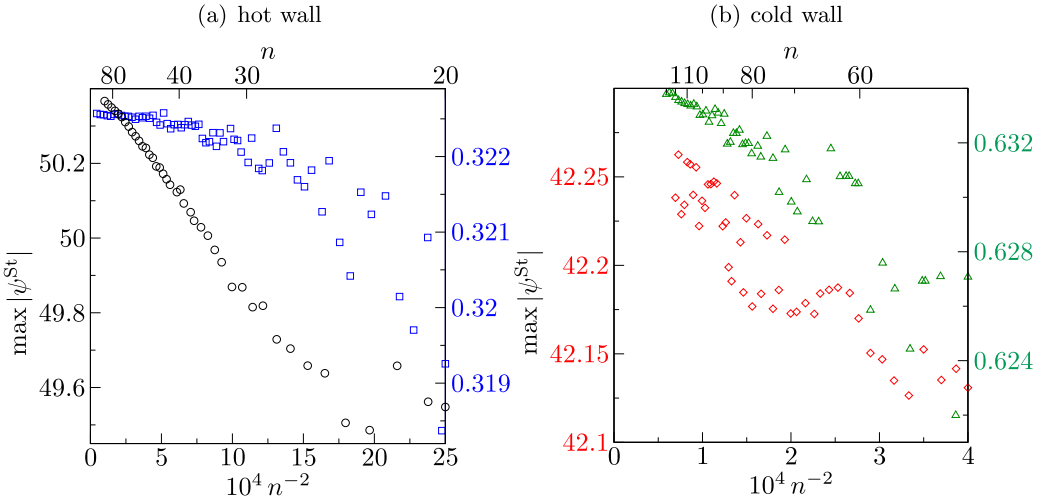

FIG. 3. Convergence of the extremum of the Stokes stream function $\|\psi^{\mathrm{St}}\|_\infty$ of the basic flow with the grid resolution $n = N\sqrt{\Gamma}$ for a hot (a) and cold wall (b) and for $(\mathrm{Pr}, \alpha, \mathrm{Re}, \mathrm{Bi}) = (10^{-3}, 90^\circ, 37024, 0.236)$, $(16.36, 25^\circ, 23622, 0.236)$, $(0.038, 120^\circ, 35645, 0.236)$ and $(28.1, 120^\circ, 17115, 0.4)$ indicated by black, blue, red and green symbols, respectively.

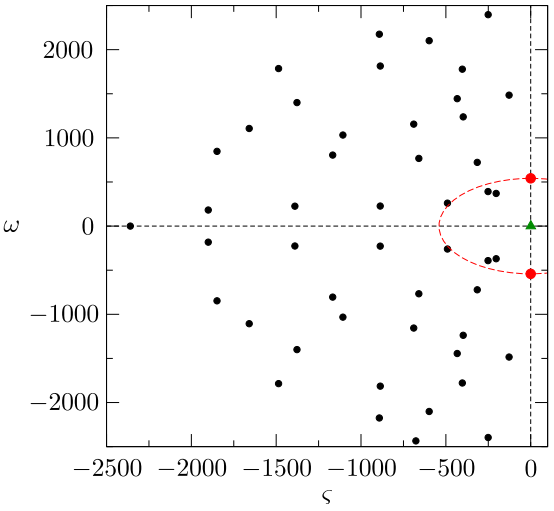

FIG. 4. The spectrum of 50 eigenvalues (dots) closest to $\sigma_A = 1 + 0\mathrm{i}$ (green triangle) for a hot wall and $(\mathrm{Pr}, \alpha, \mathrm{Re}, \mathrm{Bi}) = (10^{-3}, 90^\circ, 37024, 0.236)$. The red dashed circle indicates the distance of the leading eigenvalues (red dots) from σ_A.

close to $0 + 0\mathrm{i}$. It is recommended [51] to employ a shift σ_A with a positive real part to ensure that eigenvalues with nonnegative ς and large ω are not overshadowed by eigenvalues with small negative ς and small ω. Nevertheless, we found that even for the largest critical frequencies $\omega_c \sim \mathcal{O}(100)$ encountered in this study, there are less than 10 eigenvalues closer to the origin than the most dangerous one (Fig. 4). Thus, the most dangerous mode would be captured safely with 50 computed eigenvalues, even without the shift. If a smaller number of computed eigenvalues was desired for the sake of computational efficiency, then the real part of σ_A should be proportional to the absolute value of the critical frequency, or even a more robust algorithm of Meerbergen, Spence and Roose [52] could be adopted as in Ref. [53]. For the present problem, the small constant shift $\sigma_A = 1 + 0\mathrm{i}$ was sufficient. The matrix-vector multiplications required by ARPACK were parallelized with OpenBLAS [54].

The critical Reynolds number Re_c was sought with the iterative root-finding algorithm of Muller [55]. Assuming several critical Reynolds numbers on the critical curve as function of a governing parameter, say the Prandtl number Pr, have already been obtained, the parameter Pr is advanced. The critical Reynolds number for the advanced parameter is then calculated by a modified secant method. The two required initial guesses for Re_c are obtained from a second-order polynomial extrapolation in Pr of Re_c from previously computed points on the same critical curve and by a single Newton step for $\varsigma(\mathrm{Re})|_{\mathrm{Re}_c} = 0$ based on a zeroth-order polynomial extrapolation in Pr of $\partial\varsigma/\partial\mathrm{Re}$. Thereafter, each new estimate for Re_c is obtained as the root of the second-order interpolating polynomial of the last three computed values of $\varsigma(\mathrm{Re})$. The iterations are terminated when the error estimate $\varepsilon = |\varsigma|\partial\mathrm{Re}/\partial\varsigma$ for Re_c drops below a tolerance of 1‰.

B. Grid convergence

The grid convergence of the critical Reynolds number is demonstrated in Fig. 5 for selected cases. For a hot wall and $(\mathrm{Pr}, \alpha) = (16.36, 16^\circ)$ [blue in Fig. 5(a)] the critical Reynolds number $\mathrm{Re}_c \sim \mathcal{O}(10^3)$ is comparatively low and it is already converged to 0.1‰ deviation from a quadratically extrapolated value for an infinitely fine mesh, even on a relatively coarse mesh $N = 60/\sqrt{\Gamma}$. For a very low Prandtl number and a larger contact angle $(\mathrm{Pr}, \alpha) = (10^{-3}, 90^\circ)$ [black in Fig. 5(a)], the critical Reynolds number $\mathrm{Re}_c \sim \mathcal{O}(10^4)$ is one order of magnitude larger compared to the case $(\mathrm{Pr}, \alpha) = (16.36, 16^\circ)$. The deviation is then approximately 5‰ with $N = 60/\sqrt{\Gamma}$ and 3‰ with $N = 80/\sqrt{\Gamma}$.

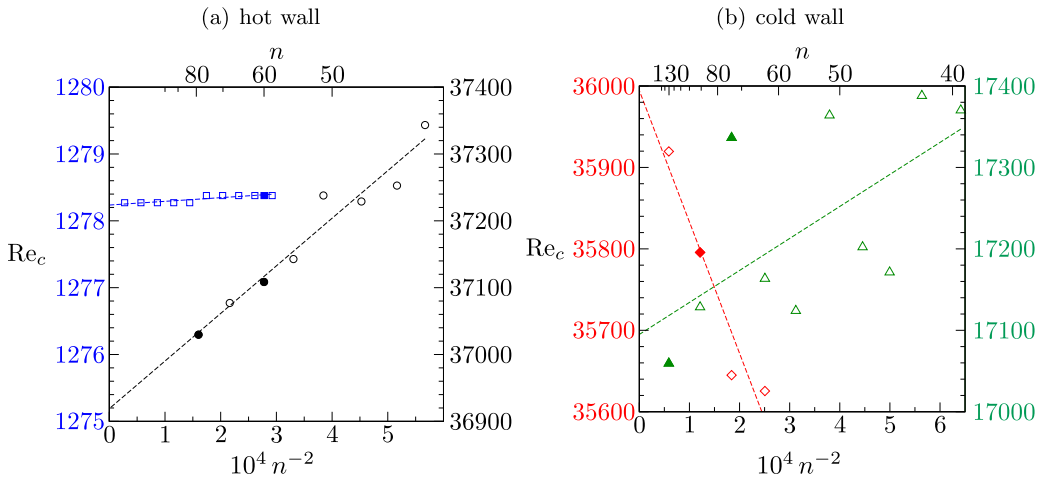

FIG. 5. Convergence of Re_c with $n = N\sqrt{\Gamma}$. (a) Hot wall, $\mathrm{Bi} = 0.236$ and $(\mathrm{Pr}, \alpha) = (10^{-3}, 90^\circ)$ and $(16.36, 16^\circ)$ indicated by black circles and blue squares, respectively. (b) Cold wall with $\alpha = 120^\circ$ and $(\mathrm{Pr}, \mathrm{Bi}) = (0.038, 0.236)$ (red diamonds) and $(28.1, 0.4)$ (green triangles). The dashed lines are least-squares linear fits of $\mathrm{Re}_c(n^{-2})$. The solid symbols correspond to the grid resolutions mentioned in the text.

In the case of a cold wall, a finer mesh is required to obtain Re_c with sufficient accuracy. For a low Prandtl number and a large contact angle $(\mathrm{Pr}, \alpha, \mathrm{Bi}) = (0.038, 120^\circ, 0.236)$ [red in Fig. 5(b)], the deviation is 6‰ with $N = 90/\sqrt{\Gamma}$. For larger Prandtl and Biot numbers $(\mathrm{Pr}, \mathrm{Bi}) = (28.1, 0.4)$ [green in Fig. 5(b)], the nonmonotonicity with respect to the resolution N due to the unstructured nature of the grid is clearly visible on the scale of the plot. For these parameters, large velocity and temperature gradients are concentrated near the contact line $(r, z) = (1, 0)$. Nevertheless, the amplitude of the variation of Re_c with N is only within 8‰ for $N \in [73/\sqrt{\Gamma}, 130/\sqrt{\Gamma}]$.

C. Code verification

To check the correct implementation of our code we consider the linear stability of the thermocapillary flow in a thermocapillary liquid bridge with a statically deformed free surface under zero gravity conditions which is heated differentially [56]. This problem is selected because linear stability results are available. The surface shape is computed as in Nienhüser and Kuhlmann [56] and the mesh is constructed and refined analogously to the droplet. The number of element edges constituting the free surface is set to $N^2/16$. The elements adjacent to the walls are split into halves, while each element within the distance (scaled with the radius of the concentric solid disks supporting the liquid bridge) of 0.04 and 0.01 from the cold corner are divided into 8 and 64 pieces for $\mathrm{Pr} < 1$ and $\mathrm{Pr} \geqslant 1$, respectively.

The critical Reynolds numbers obtained for $\Gamma = 1$, $\mathrm{Bi} = 0$, two Prandtl numbers Pr, and different contact angles α are shown in Table I as a function of the grid resolution. In all cases, the critical wave number is $m = 2$. Our results for Re_c compare very well with the reference results of Nienhüser and Kuhlmann [56]. The deviations from the reference results found are typically $\approx$1% (for $N = 100$), except for the deviation of $\approx$5% in the demanding case of $(\mathrm{Pr}, \alpha) = (0.02, 130^\circ)$. The agreement between the oscillation frequencies ω_c for $\mathrm{Pr} = 4$ (not shown) is on a similar level. For $\mathrm{Pr} = 0.02$ the instability is stationary.

Linear stability results for the present model of a nonvolatile wall-attached droplet are not yet available from other authors. Nevertheless, we attempt a comparison with the results of Shi *et al.* [35] who carried out full three-dimensional time-dependent numerical simulations including radiation heat transfer at the free surface. To that end the thermal boundary condition is supplemented with

TABLE I. Critical Reynolds number Re_c of the axisymmetric thermocapillary flow in a noncylindrical liquid bridge with aspect ratio $\Gamma = 1$ under zero gravity for different contact angles α and two different Prandtl numbers Pr. The critical wave number is $m = 2$ in all cases.

Pr		0.02			4		
N \ α		50°	90°	130°	50°	90°	130°
40		2426	2058	2930	1458	1001	805
60		2411	2058	2911	1452	1001	807
80		2408	2059	2907	1451	1001	808
100		2405	2059	2902	1449	1001	808
[56]		2380	2060	3070	1445	1010	800
[53]						1002	

a Stefan-Boltzmann law as described in Appendix A, based on the thermophysical parameters provided by Shi *et al.* [35]. While the full nonlinear radiation law is used for the basic state, the linearization used for the perturbation flow leads to a lump Biot number $\mathrm{Bi}_{\mathrm{lump}} = \mathrm{Bi} + 4\mathrm{Bi}_{\mathrm{r}} = 0.202 + 4 \times 0.0342 = 0.339$, where Bi_{r} is a radiation Biot number as explained in Appendix A. A comparison between the critical Marangoni numbers is made in Fig. 6. It should be noted that Shi *et al.* [35] specified an *a posteriori* effective Biot number $\mathrm{Bi}_{\mathrm{eff}} = 0.438$ for their simulations which was evaluated at some supercritical flow conditions far above the stability boundary, combining conduction, convection, and radiation. This value cannot be directly compared to the *a priori* lump Biot number $\mathrm{Bi}_{\mathrm{lump}}$ imposed by the thermal boundary conditions. The critical Marangoni numbers for $\alpha \leqslant 15°$ are in good agreement, although the critical Marangoni numbers specified by Shi *et al.* [35] (blue triangles in Fig. 6) are slightly smaller than the present linear stability results for $\mathrm{Bi} = 0.339$ (lines). This deviation can be explained as follows. The stationary $m = 0$ modes (blue triangles in Fig. 6) did not arise due to symmetry-breaking instabilities. The $m = 0$ modes detected by Shi *et al.* [35] rather characterize the onset of a different stationary axisymmetric flow with concentric rolls embedded in the global axisymmetric circulation. In Sec. IV A 1 below we show for $\alpha = 5°$ and $\mathrm{Bi} = 0.236$

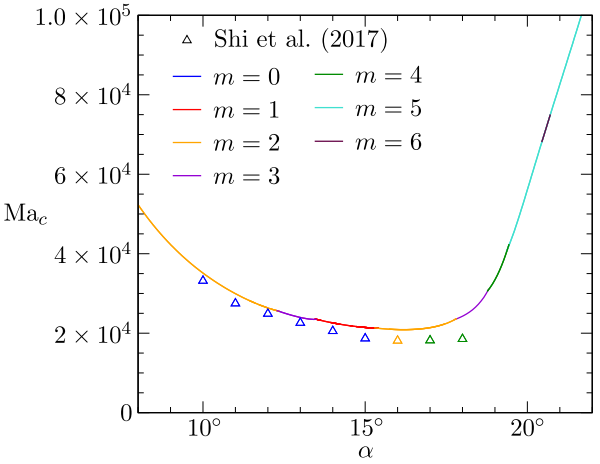

FIG. 6. Dependence of the critical Marangoni number Ma_c on the contact angle α for a hot wall, $\mathrm{Pr} = 16.36$ and a superposition of Newton's and Stefan-Boltzmann's law according to the thermophysical parameters and conditions provided by Shi *et al.* [35]. Full lines: present linear stability analysis. Symbols: results of Shi *et al.* [35] for the same material parameters. Different wave numbers are indicated by color.

(disregarding radiation) that a symmetry-preserving saddle-node bifurcation of the basic flow exists at Reynolds numbers below the one for the symmetry-breaking instability (corresponding to the lines in Fig. 6). While such saddle-node bifurcations are not easily tracked by time-dependent numerical simulations, they could be responsible for the blue triangles marking axisymmetric flow transitions in Fig. 6. For $\alpha > 15^\circ$ the most dangerous modes are nonaxisymmetric (orange and green triangles for the results of Shi *et al.* [35]) and the deviations between both results grow. One possible reason for these deviations of the critical Marangoni numbers could be subcritical bifurcations. As shown below in Sec. IV A 2, the neutral curves for different wave numbers are fairly close to each other and intersect in the range $\alpha \in [15^\circ, 20^\circ]$ which may lead to a complicated nonlinear interaction.

According to our linear stability analysis, the most dangerous (infinitesimal) symmetry-breaking perturbation mode is nonaxisymmetric and steady up to $\alpha = 13.5^\circ$, while for higher contact angles the critical modes are oscillatory. In contrast, Shi *et al.* [35] predict a steady axisymmetric multi-cell flow (created by a basic flow bifurcation) up to $\alpha = 15^\circ$. The close agreement between the critical Marangoni numbers for $\alpha \leqslant 15^\circ$ provides confidence in the current code.

For the results presented in the following sections, as a compromise between effort and accuracy, we select $N = 80/\sqrt{\Gamma}$ for a hot substrate, $N = 90/\sqrt{\Gamma}$ for a cold substrate and $\mathrm{Pr} < 1$, and $N = 110/\sqrt{\Gamma}$ for a cold substrate and $\mathrm{Pr} \geqslant 1$. Linear stability results for droplets attached to a hot wall are presented first, followed by those for droplets attached to a cold wall.

IV. DROPLETS ON A HOT WALL

A. Shallow high-Prandtl-number droplet

As a representative high-Prandtl-number fluid we consider in this section $\mathrm{Pr} = 16.36$ and Biot number $\mathrm{Bi} = 0.236$, corresponding to a droplet from 1 cSt silicone oil, the wetting radius of $R = 2.5 \times 10^{-3}$ m, and the heat transfer coefficient of $h_c = 9.44$. These parameters correspond to those of Shi *et al.* [35], but with radiation disregarded and with a higher value of the heat transfer coefficient. As mentioned in Sec. II A the asymptotic limit $\mathrm{Bd} \to 0$ is considered throughout, unless stated otherwise.

1. Two-dimensional steady flows

a. Global thermocapillary flow. For a droplet on a hot substrate in a cold environment, the surface temperature will decay from the contact line toward the apex of the droplet. The resulting axisymmetric thermocapillary flow is thus directed from the contact line to the apex of the droplet and returns to the region near the contact line along the hot wall. Examples of the basic flow at the critical Marangoni number for the onset of three-dimensional flow are shown in Fig. 7 for contact angles $\alpha \leqslant 25^\circ$.

The thermocapillary flow is characterized by a single toroidal vortex. For large contact angles [Figs. 7(c) and 7(d)] the toroidal flow is strong (Table II). As the contact angle becomes smaller, the flow becomes weaker and it develops a circular hyperbolic line of stagnation in the range $12^\circ \lesssim \alpha \lesssim 17^\circ$. For $\alpha = 15^\circ$ [Fig. 7(b)] the stagnation line is located at $(r, z) = (0.187, 0.083)$.

For still smaller contact angles $\alpha < 10^\circ$ the flow gets weaker and the temperature field becomes almost conducting, depending nearly linearly on z. Therefore, the tangential thermocapillary stresses, vanishing at $r = 0$, are very small in a region around the apex of the droplet and the fluid is almost quiescent in this region.

b. Axisymmetric Marangoni instability. As an example for a shallow high-Prandtl-number droplet heated from the wall we consider $\alpha = 5^\circ$ in some more detail. The global thermocapillary flow driven by the temperature difference between the wall and the apex of the droplet is very weak and almost quiescent. As the Marangoni number Ma_H exceeds a critical value we find steady axisymmetric concentric convection rolls due to a Marangoni instability.

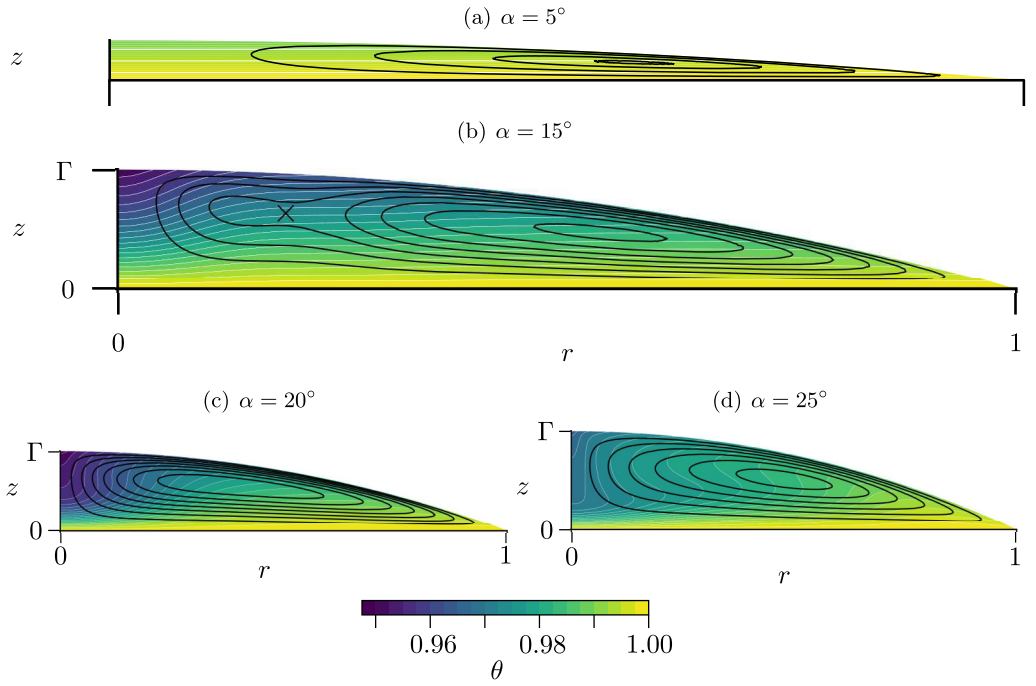

FIG. 7. Streamlines (black) and temperature field (color and white isotherms) of the basic flow at criticality for a droplet of $\mathrm{Pr} = 16.36$ on a hot surface and (a) $\alpha = 5°$, $\mathrm{Ma}_{H,c} = 83.35$, (b) $\alpha = 15°$, $\mathrm{Ma}_{H,c} = 122.0$, (c) $\alpha = 20°$, $\mathrm{Ma}_{H,c} = 603.3$, (d) $\alpha = 25°$, $\mathrm{Ma}_{H,c} = 4263$. The cross $\times$ in panel (b) indicates the position of a hyperbolic stagnation point found with the Newton-Raphson method.

A bifurcation diagram in terms of the vertical velocity $w_0(r = 0, \Gamma/2)$ on the axis at midheight is shown in Fig. 8. For $\mathrm{Ma}_H \lesssim 80$ the basic flow (full orange line) corresponding to the global thermocapillary flow is unique and weak on the scale shown with $w_0(r = 0, \Gamma/2) < 0$. At $\mathrm{Ma}_{H,c}^{\mathrm{2D}} = 83.18$ (diamond in Fig. 8) additional solutions corresponding to steady axisymmetric concentric convection rolls bifurcate transcritically from the basic flow. The bifurcating convection rolls are much stronger at $r = 0$ than the global thermocapillary-driven flow. The subcritically bifurcating solution branch (blue) has up-flow on the axis (except near the transcritical bifurcation point). It is unstable (dashed blue line) in two dimensions and becomes two-dimensionally stable (solid blue line) at the saddle-node bifurcation point $(\mathrm{Ma}_H^{\mathrm{SN}}, w(0, \Gamma/2)) = (82.16, 0.479)$ (square in Fig. 8). The solution bifurcating supercritically from the transcritical bifurcation point has downflow on the axis initially. For higher $\mathrm{Ma}_H > \mathrm{Ma}_{H,c}^{\mathrm{2D}}$, $w_0(r = 0, \Gamma/2)$ oscillates with Ma_H.

In the absence of the weak global thermocapillary flow the transcritical bifurcation (diamond in Fig. 8) would be perfect. The bifurcation diagram suggests that in that case $w_0(r = 0, \Gamma/2)$ of the supercritically bifurcating solution would oscillate about $w_0 = 0$ creating a sequence of transcritical bifurcations. Here, the weak global flow represents a perturbation to these transcritical bifurcations

TABLE II. Maximum velocity magnitude of the basic thermocapillary flow at the critical Marangoni number (as in Fig. 7) versus the contact angle for a hot wall, $\mathrm{Pr} = 16.36$ and $\mathrm{Bi} = 0.236$.

α	10°	15°	20°	25°
max $\lvert\boldsymbol{u}\rvert$	1.06	3.01	11.51	29.92

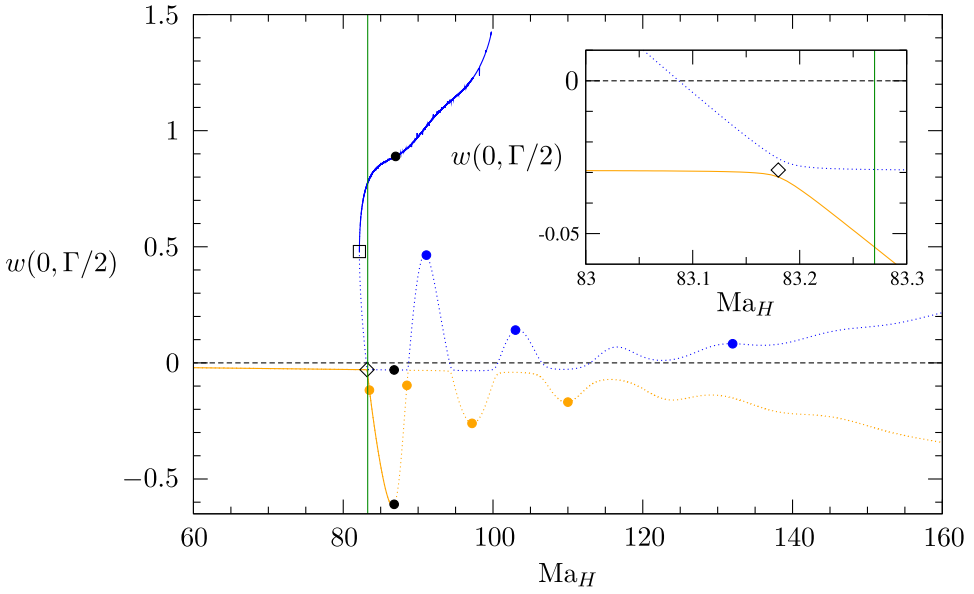

FIG. 8. Imperfect bifurcations for heating from the wall, Pr = 16.36 and $\alpha = 5^\circ$ showing the vertical velocity $w_0(r = 0, z = \Gamma/2)$ on the axis and at mid-height as a function of Ma_H. The connected and disconnected solution branches are shown in orange and blue, respectively. Full (dotted) lines indicate solutions which are stable (unstable) to axisymmetric perturbations. The black square marks the saddle node bifurcation point, the diamond shows the (weakly perturbed) transcritical bifurcation point. Flow fields at the black dots are shown in Fig. 9. Flow fields at the colored dots are discussed in Fig. 36 in Appendix D. The vertical green line indicates the critical Marangoni number for the three-dimensional symmetry-breaking instability (from Fig. 10) of the two-dimensionally stable solution (full orange line). The inset shows a zoom into the region near the perturbed transcritical bifurcation.

of the convection rolls such that the bifurcations are imperfect. The first transcritical bifurcation is only slightly perturbed (inset in Fig. 8). In this sense, the perfect bifurcation point (diamond) specified above as $\mathrm{Ma}_{H,c}^{\mathrm{2D}} = 83.18$ represents an approximation. As Ma_H increases and the global thermocapillary flow becomes stronger, the transcritical bifurcations become increasingly perturbed such that the connected (orange) and disconnected (blue) solutions separate from each other (for $\mathrm{Ma}_H \gtrsim 120$).

A similar Marangoni instability from the state of rest is found in liquid pools [57]. The degeneracy of the two equivalent solutions with either up- or down-flow on the axis is removed by nonlinear finite-amplitude effects (and in the present case by the curvature of the interface) such that the bifurcation of concentric Marangoni rolls for zero gravity is transcritical. For a pool with depth-to-radius ratio $\Gamma = 1/1.8$ and zero tangential vorticity on the adiabatic cylindrical side walls, Rosenblat, Homsy and Davis [57] find the transcritical bifurcation at $\mathrm{Ma}_H = 79.7$. This value compares well with the present value of $\mathrm{Ma}_{H,c}^{\mathrm{2D}} = 83.18$. Also, the flow directions are the same for the present high-Prandtl-number flow and flow in cylindrical pools. For very shallow pools, Schatz *et al.* [58] experimentally found the transcritical bifurcation at $\mathrm{Ma}_H = 83.6$. This is only 0.5% larger than the present value of $\mathrm{Ma}_{H,c}^{\mathrm{2D}}$. The deviation is well within the error bar $\Delta\mathrm{Ma}_{H,c} = \pm 11$ specified by Schatz *et al.* [58]. Also, the range of $\epsilon := (\mathrm{Ma}_H^{\mathrm{SN}} - \mathrm{Ma}_{H,c}^{\mathrm{2D}})/\mathrm{Ma}_{H,c}^{\mathrm{2D}} = -1.22 \times 10^{-2}$ over which the basic flow and the disconnected branch solution (past the saddle-node) are both linearly stable in two-dimensions has a similar magnitude as the corresponding value -3.2×10^{-2} in the experiments. Different from the experiments by Schatz *et al.* [58], who found the stable bifurcating flow to arise in form of regular hexagons, we find concentric rolls. This difference is attributed to

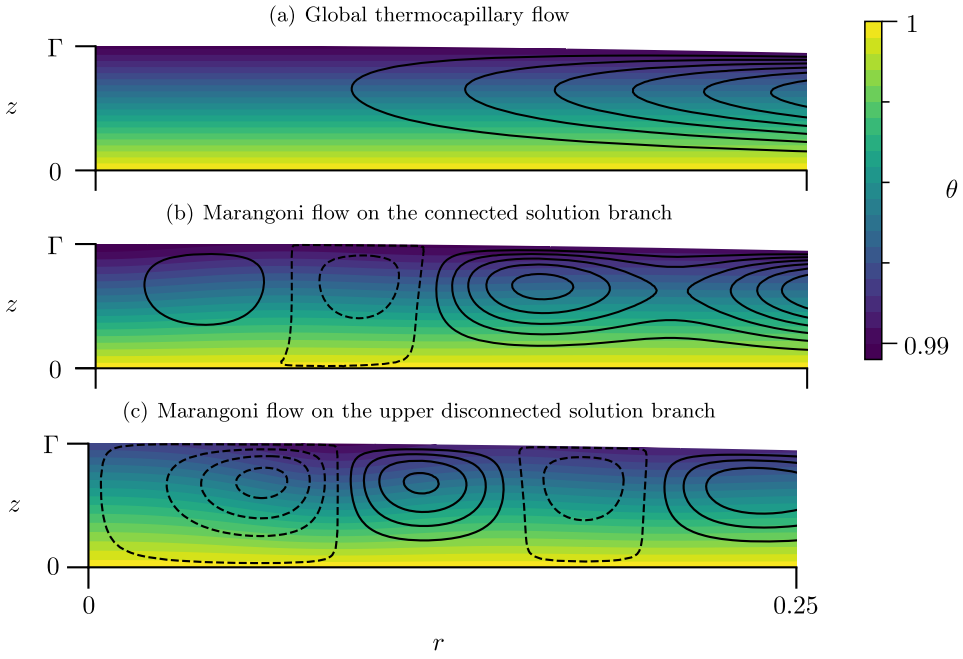

FIG. 9. Two-dimensional flows for heating from the wall, $\mathrm{Pr} = 16.36$, $\alpha = 5^\circ$ and $\mathrm{Ma}_H = 87$ (three vertically aligned black dots in Fig. 8). (a) the lower branch of the disconnected solution corresponding to the global thermocapillary flow (for $\mathrm{Ma}_H = 87$), (b) Marangoni rolls on the connected solution branch, and (c) Marangoni rolls on the disconnected solution branch.

the shape of the droplet for which the local Marangoni number $\mathrm{Ma}_{\mathrm{loc}}(r) := \mathrm{Ma}_H[h(r)/H]$, based on the local height $h(r)$, depends on r and, for slightly supercritical driving, drops to subcritical values beyond a critical distance r^* from the axis. As a result, the concentric Marangoni rolls are localized and centered at the axis.

For $\mathrm{Ma}_H = 87$ Fig. 9 compares the unstable global thermocapillary flow corresponding (at this Marangoni number) to the lower branch of the disconnected solution (a), the marginally stable (in 2D) connected-branch Marangoni rolls (b), and the stable (in 2D) upper-branch Marangoni rolls of the disconnected solution (c) (three black dots in Fig. 8). Apparently, the disconnected upper-branch Marangoni-flow solution with up-flow on the axis is favored by the concave shape of the interface and exhibits the strongest (positive) velocity on the axis $r = 0$. This flow is stable in two dimensions and its strength (as well as the radial extension) increases rapidly with Ma_H. In contrast, the lower branch of the disconnected solution is always unstable in 2D, as is the flow on the connected solution branch for $\mathrm{Ma}_H > 87.0$. Despite their instability, the oscillating character of the flow direction with respect to a variation of Ma_H is intriguing. Therefore, some related considerations are provided in Appendix D.

As the contact angle (aspect ratio) increases, the thermocapillary flow becomes stronger. Associated with it is an increased perturbation of the locally almost conducting state near the apex. As a result, the two-dimensional bifurcation to concentric Marangoni rolls becomes increasingly perturbed and the saddle node of the disconnected solution branch moves to higher Marangoni numbers. For $\alpha = 15^\circ$ we could no longer find numerically the disconnected solution branch. In the following, we investigate the three-dimensional instability of the dominant connected solution for which $w_0(r = 0, z = \Gamma/2) < 0$ (down-flow on the axis).

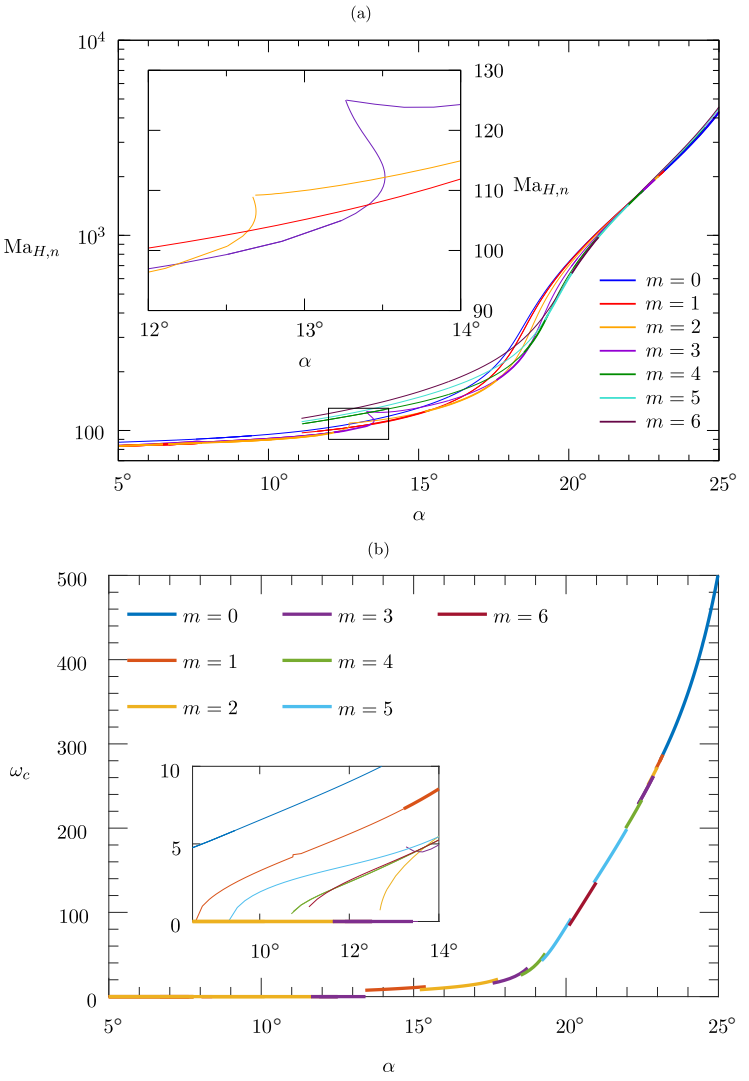

FIG. 10. Dependence of the critical (thick lines) and neutral (thin lines) Marangoni numbers (a) and the critical (thick lines) and neutral (thin lines, inset only) oscillation frequencies (b) on the contact angle α for shallow droplets on a hot substrate with $\mathrm{Pr} = 16.36$.

2. Three-dimensional flow instability

For $\alpha = 5^\circ$ the steady axisymmetric connected-branch solution becomes unstable to three-dimensional perturbations at $\mathrm{Ma}_{H,c} = 83.27$ (vertical green line in Fig. 8), only slightly above the transcritical bifurcation point. At the same Marangoni number, the upper branch of the disconnected solution is linearly stable with respect to three-dimensional perturbations. Since the most dangerous mode of the upper-branch disconnected solution is found to be axisymmetric with a real growth rate of $\varsigma(m = 0, \mathrm{Ma}_H = 83.27) < 0$, we can expect the upper-branch disconnected solution to be linearly stable in a range around the critical Marangoni number of the connected-branch solution. Furthermore, since the basic subcritical flow for very low Ma_H merges smoothly into the connected solution, in particular for $\alpha > 5^\circ$, we investigate the three-dimensional instability of the connected solution, also denoted *basic state* in the following. The corresponding critical Marangoni number is

TABLE III. Neutral Marangoni numbers $\mathrm{Ma}_{H,n}$ for different azimuthal wave numbers m for a droplet on a hot substrate with contact angle $\alpha = 5^\circ$ and Prandtl number $\mathrm{Pr} = 16.36$. The $m = 0$ mode is oscillatory with $\omega_n = 4.36$.

m	0	1	2	3	4	5	6	7	8
$\mathrm{Ma}_{H,n}$	87.01	83.27	83.35	83.92	84.47	85.18	87.04	86.82	87.55

denoted $\mathrm{Ma}_{H,c}$. As long as an axisymmetric upper branch of the disconnected solution stably exists in a range of $\mathrm{Ma} > \mathrm{Ma}_{H,c}$ the supercritical flow could possibly be bistable between the steady concentric Marangoni roll solutions of the upper branch of the disconnected solution and a slightly supercritical three-dimensional flow near the unstable connected-branch solution.

The critical curve $\mathrm{Ma}_{H,c}(\alpha)$ for the basic state and $\alpha > 5^\circ$ is shown in Fig. 10(a). Similar to the critical onset in cylindrical liquid pools [59], the neutral Marangoni numbers for different azimuthal wave numbers are very close to each other. For $\alpha < 8^\circ$ the critical curves for the azimuthal wave numbers $m = 1$ and $m = 2$ are almost indistinguishable. As a result, the critical wave number often changes with the contact angle. Increasing α from 15° to 20.5°, the critical wave number monotonically increases from 1 to 6. A further increase of α leads to a monotonic reduction of m until, for $\alpha \gtrsim 23.1^\circ$, the critical mode has become axisymmetric ($m = 0$). The critical Marangoni number $\mathrm{Ma}_{H,c}$ is a strictly monotonic function of α within the range considered. Extrapolating the critical Marangoni number $\mathrm{Ma}_{H,c}$ to $\alpha \to 0^\circ$ we find $\mathrm{Ma}_{H,c}(\alpha = 0) \approx 79.6$ by quadratic extrapolation the critical data of the $m = 2$ mode. This is a typical value for critical Marangoni numbers also found for plane liquid layers [18] and shallow pools [44,57].

The critical three-dimensional modes are all stationary for $\alpha < 13.4^\circ$ [Fig. 10(b)]. For $\alpha = 5^\circ$ the basic state becomes unstable at $\mathrm{Ma}_{H,c} = 83.27$ to a nonaxisymmetric steady mode with $m = 1$. Further neutral Marangoni numbers for $m \in [0, 8]$ are provided in Table III. For $m \geqslant 1$, they increase with the azimuthal wave number m and demonstrate the crowding of neutral modes. The critical and some neutral modes are shown in Fig. 11. Here and in all following figures red and blue color shading indicates $\theta' > 0$ and $\theta' < 0$, respectively. These modes as well as the stationary modes

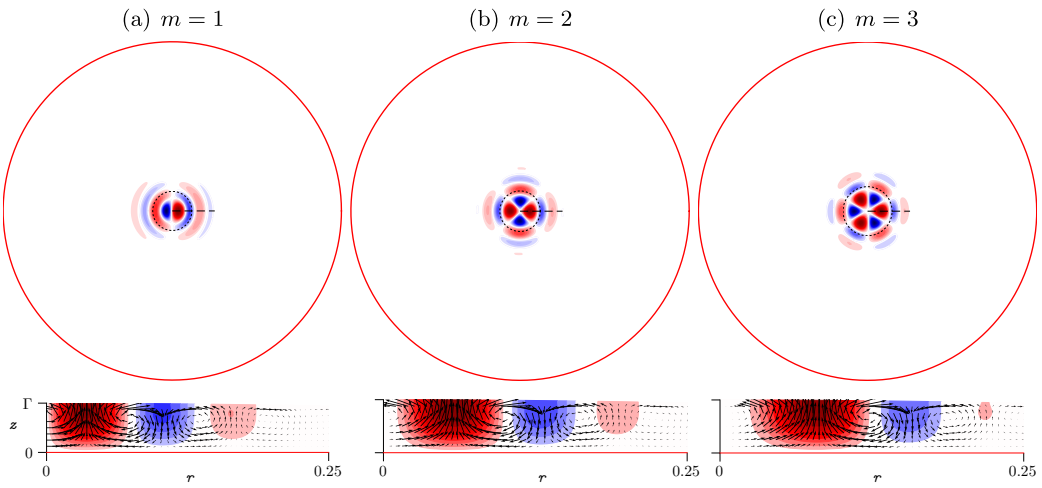

FIG. 11. Critical mode with $m = 1$ (a) and neutral modes with $m = 2$ (b) and $m = 3$ (c) for $\alpha = 5^\circ$. The critical/neutral Marangoni numbers are given in Table III. The free-surface temperature distribution is shown at the top, while at the bottom the velocity vectors and temperature field are shown close to the axis and in the plane $\varphi = 0$ (corresponding to a horizontal cut along the dashed line in the top view). The dotted circles in the top views indicate the critical distance r^* from the axis where $\mathrm{Ma}_{\mathrm{loc}}(r^*) = \mathrm{Ma}_H^{\mathrm{SN}} = 82.16$.

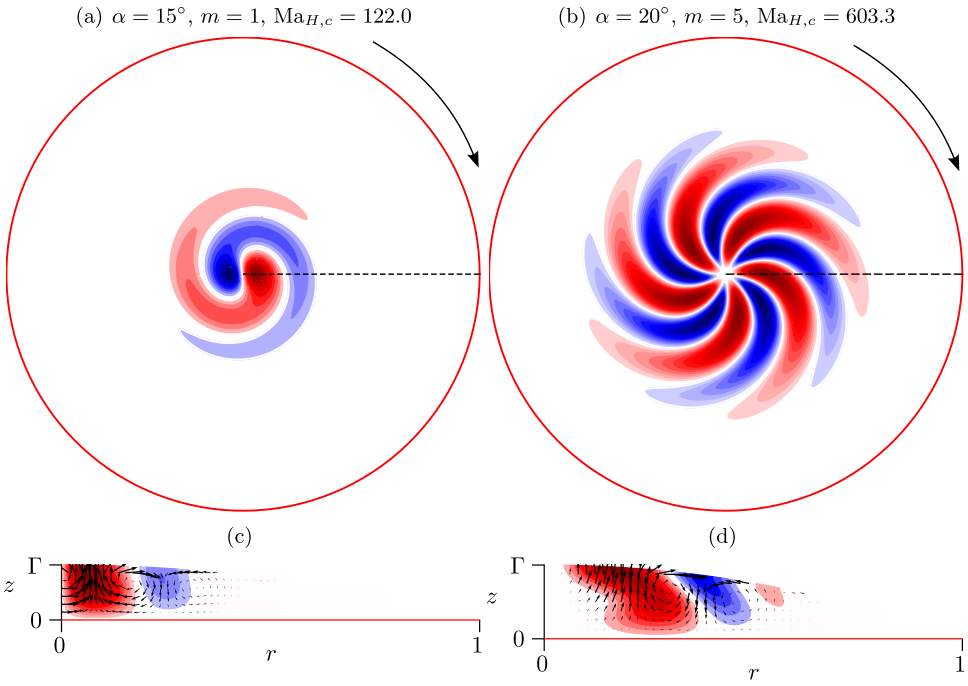

FIG. 12. Critical modes for a droplet on a hot substrate with Pr = 16.36 and $\alpha = 15°$ (a), (c) and $\alpha = 20°$ (b), (d). The critical Marangoni and wave numbers are $\mathrm{Ma}_H = 122.0$, $m = 1$ and $\mathrm{Ma}_H = 603.3$, $m = 5$, respectively. The surface temperature is shown in panels (a), (b), while the velocity and temperature field are shown in panels (c), (d) in a plane $\varphi = \text{const.}$ containing the maximum positive temperature perturbation in the bulk. The waves rotate clockwise.

for other small values of α are localized near $r = 0$ and exhibit a clear cellular structure in the cross-section of constant φ, similar to the axisymmetric basic state for $\mathrm{Ma}_{H,c} > \mathrm{Ma}_{H,c}^{2\mathrm{D}}$. Therefore, these three-dimensional instabilities must also be due to a Marangoni instability in which the temperature perturbations are produced by the vertical advection of basic temperature by the perturbation flow. Furthermore, as α increases, the critical modes extend further in the radial direction.

Since the neutral curves for the steady low-α modes $m = 2$ and $m = 3$ turn backward [inset in Fig. 10(a)] upon an increase of α at $\alpha = 12.7°$ and $\alpha = 13.3°$, respectively, the stationary mode with wave number $m = 3$ is replaced by the oscillatory mode with $m = 1$ at a codimension-two point at $\alpha = 13.4°$. This transition from stationary to oscillatory critical modes seems to suggest a modification of the instability mechanism. The critical circular frequencies ω_c [Fig. 10(b)] grow monotonically with α. Since the time-dependent critical modes arise in complex conjugate pairs, we only present clockwise rotating modes as viewed from above the droplet. For these modes $\omega > 0$ for $m \geqslant 1$. Examples of oscillatory critical modes are shown in Fig. 12 for $\alpha = 15°$ and $20°$. For the purpose of illustration Fig. 13 shows a superposition of the basic states at criticality and the same critical modes with arbitrary amplitudes. The temperature perturbation exhibits a fan-blade shape distribution on the free surface, similar to that observed by Karapetsas *et al.* [39] in shallow evaporating droplets on a perfectly conducting substrate. Therefore, the temperature perturbation structures close to the axis lag those near the periphery. Owing to the strong winding of the spirals the perturbation flow in azimuthal cross sections at constant φ has a cellular character, as for the low-α stationary modes, but the cells at constant φ appear to travel radially inward, related to the (negative) azimuthal direction of wave propagation. The structure of the critical mode for $\alpha = 15°$ is consistent with the flow oscillations simulated by Shi *et al.* [35] (their Fig. 7), who obviously found a nonlinear standing wave composed of the two bifurcating counter-propagating waves of

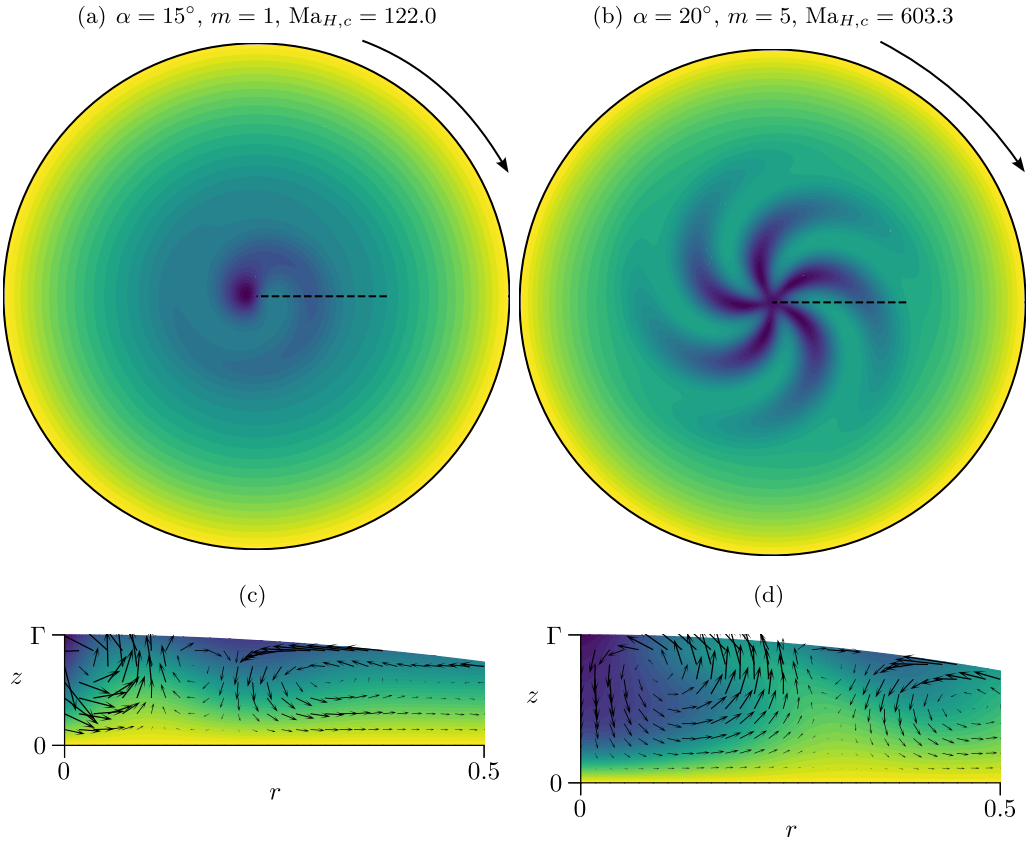

FIG. 13. Superposition of the basic states and the corresponding critical modes for the same parameters as in Fig. 12. The amplitude of the perturbation flow is selected for visualization purposes such that the maximum temperature does not exceed the temperature of the wall. The top row (a), (b) shows the temperatures on the free surface, while the bottom row (c), (d) shows meridional cuts along the dashed lines. The yellow and violet borders of the colormap correspond to the maximum and minimum fluid temperature within the droplet. Arrows in panels (c), (d) represent velocity vectors.

which one is shown in Fig. 12(a). With increasing α the inward propagating cells at constant φ become increasingly oblique [Figs. 12(c) and 12(d)], an effect caused by the increasing shear in the basic flow [Figs. 7(b) and 7(c)]. Since the basic flow also develops considerable radial temperature gradients, the rotating critical modes combine characteristics of the (stationary) Marangoni instability [18] and of (oscillatory) hydrothermal waves [19]. Both mechanisms are based on basic state temperature gradients in the bulk and a feedback through the thermocapillary-induced perturbation flow.

An example of an axisymmetric ($m = 0$) oscillatory critical mode at an even larger contact angle $\alpha = 25°$ is shown in Fig. 14. The perturbation streamlines and temperature field are displayed at four instants over half a period $\tau/2 = \pi/\omega_c$ of oscillation. The perturbation flow consists of concentric convection rolls which propagate radially inward. Rolls are generated near the contact line and they are annihilated on the axis. Despite the increased importance of radial temperature gradients of the basic flow for this larger contact angle [Fig. 7(d)], the basic state temperature gradients normal to the interface dominate. From the extrema of the perturbation temperature near the free surface between the concentric rolls, it is obvious that the traveling concentric rolls are supported by the classical Marangoni effect [18], except near the axis where radial temperature gradients dominate in the

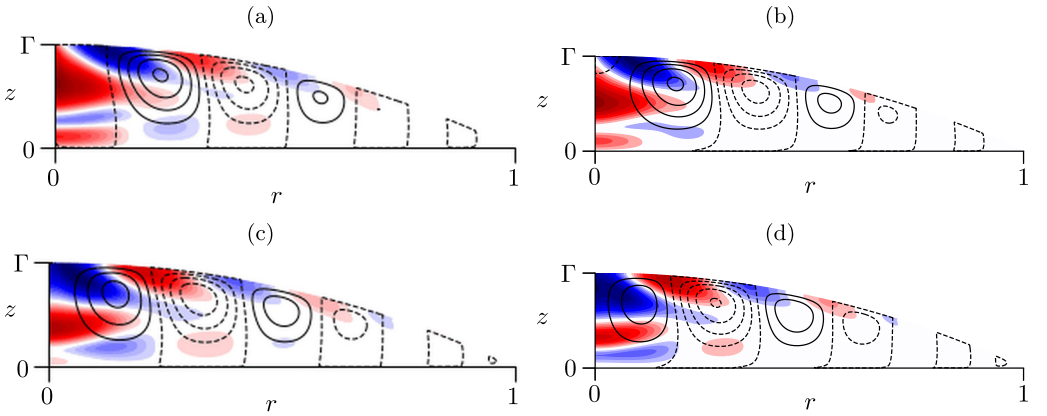

FIG. 14. Critical axisymmetric mode ($m = 0$) for $\alpha = 25^\circ$ with $\mathrm{Ma}_{H,c} = 4263$ and $\omega_c = 503$. Shown are snapshots of the perturbation temperature and streamfunction at times t_0 (a), $t_0 + \tau/8$ (b), $t_0 + \tau/4$ (c), and $t_0 + 3\tau/8$ (d), where $\tau = 2\pi/\omega_c$ is the period of oscillation.

basic state and the behavior is more complex. Even though the mechanism is mixed, we shall call this mode radially propagating Marangoni rolls. Since the temperature perturbations at mean radial coordinates $r \approx 0.5$ arise near the interface (not in the bulk) the inward propagation of the critical mode seems to be due to the radially inward advection provided by the basic free surface flow. In fact, the radial phase velocity compares well with the free surface velocity $w_0(r, h(r))$. For example, the mean radial propagation velocity of the maximum of the free-surface perturbation temperature between Figs. 14(a) and 14(d) is -30, while the radial velocity of the basic flow at the location of the maximum perturbation temperature varies from $u_0 = -28$ [Fig. 14(a)] to $u_0 = -29$ [Fig. 14(d)].

The stability threshold $\mathrm{Ma}_{H,c}$ of the present high-Prandtl-number basic flow for heating from the wall increases approximately exponentially with α [note the logarithmic scale in Fig. 10(a)]. As α increases the thermocapillary flow gets stronger and, for a high Prandtl number, the vertical temperature profile becomes strongly S-shaped with a local inversion of the temperature gradient [Fig. 7(d)]. Therefore, temperature perturbations associated with velocity perturbations in form of a regular roll structure, which extends vertically over the full depth of the liquid, can be amplified by vertical advection of basic state temperature via the Pearson mechanism only over a relatively thin subsurface layer within which $\partial_z \theta_0 < 0$. However, the intermediate layer with the inverted temperature gradient $\partial_z \theta_0 > 0$ acts stabilizing regarding the Pearson mechanism. This structural change of the basic flow with an inverted vertical temperature gradient may explain the strong increase of $\mathrm{Ma}_{H,c}$ with α.

The types of instabilities, stationary cells, rotating patterns, and radially propagating rolls, found for $\mathrm{Pr} = 16.36$ are also expected for other high-Prandtl-number droplets when the heating is from the wall. For $\alpha = 16^\circ$ the dependence of the critical Marangoni number on the Prandtl number is shown in Fig. 15. For this contact angle, rotating spirals with $m = 1$ or $m = 2$ can become critical. In the limit of large Prandtl numbers, the neutral Marangoni number seems to saturate. In this limit, the Reynolds number $\mathrm{Re}_H = \mathrm{Ma}_H/\mathrm{Pr} \to 0$ becomes arbitrarily small for constant Ma_H such that the basic flow field is creeping and the basic flow (including the temperature field) does not change anymore. Similar arguments apply to the perturbation flow such that $\mathrm{Ma}_{H,c}$ should indeed saturate. However, when $\mathrm{Pr} \to 0$, the critical Marangoni number seems to diverge. In this limit, the basic temperature field becomes perfectly conducting, and all instabilities which rely on temperature fluctuations are rapidly dissipated such that the critical Marangoni number must diverge for those perturbations. Merely, purely inertial instabilities remain possible in the low Prandtl number limit as, e.g., in thermocapillary liquid bridges [29,60,61] or pools [62,63].

Buoyancy has a stabilizing (destabilizing) effect in the case of a pendant (sessile) low-contact-angle droplet due to the vertical thermal stratification of the basic state [Figs. 7(a) and 7(b)].

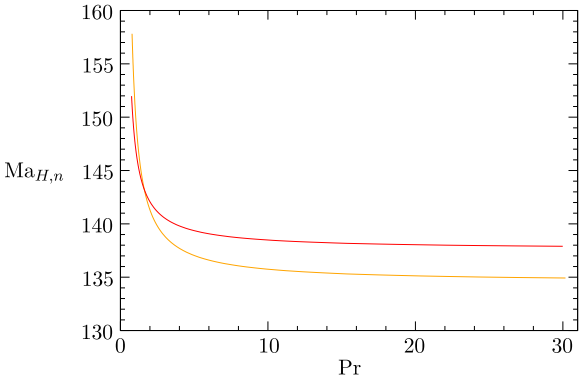

FIG. 15. Neutral curves $\mathrm{Ma}_{H,n}(\mathrm{Pr})$ for the two most dangerous modes with azimuthal wave number $m = 1$ (red) and $m = 2$ (orange) for a droplet on a hot substrate with contact angle $\alpha = 16^\circ$.

For $\alpha = 15^\circ$ and $\mathrm{Pr} = 16.36$, the critical curve $\mathrm{Ma}_{H,c}(\mathrm{Bd})$ shown in Fig. 16(a) has the slope of $\partial \mathrm{Ma}_{H,c}/\partial \mathrm{Bd}|_{\mathrm{Bd}=0} = -23.69$ at $\mathrm{Bd} = 0$. Under the physical conditions considered by Shi *et al.* [35], corresponding to $\mathrm{Bd} = 0.015$ for $\alpha = 15^\circ$, the effect of buoyancy on the critical Marangoni number is less than 3‰. Thus, it is permissible to neglect buoyancy under similar conditions. For these conditions the Rayleigh number based on the height of the droplet and the temperature difference between the wall and the free surface is $\mathrm{Ra} = \mathrm{Bd}\,\mathrm{Ma}_H \sim \mathcal{O}(1)$. This is far below the critical value $\mathrm{Ra}_c^{\mathrm{RB}} = 669$ for the onset of Rayleigh-Bénard convection in plane layers with rigid-free velocity and fixed-insulating temperature boundary conditions [64,65].

The oscillation frequencies ω_n of the neutral modes decrease monotonically with Bd [Fig. 16(b)] and eventually drop to zero. The change from an oscillating to a steady mode is accompanied by a decrease of the neutral Marangoni number. In this regard, the effect of an increase of Bd is very similar to a decrease of α. For $\mathrm{Bd} > 1.2$, the oscillating mode with $m = 1$ is replaced by a steady mode with $m = 3$, and for $\mathrm{Bd} > 2$ the azimuthal wave number decreases to $m = 2$. The same occurs when the contact angle is decreased below 13.4° and 12.2°, respectively. For $\mathrm{Bd} < -0.4$, the

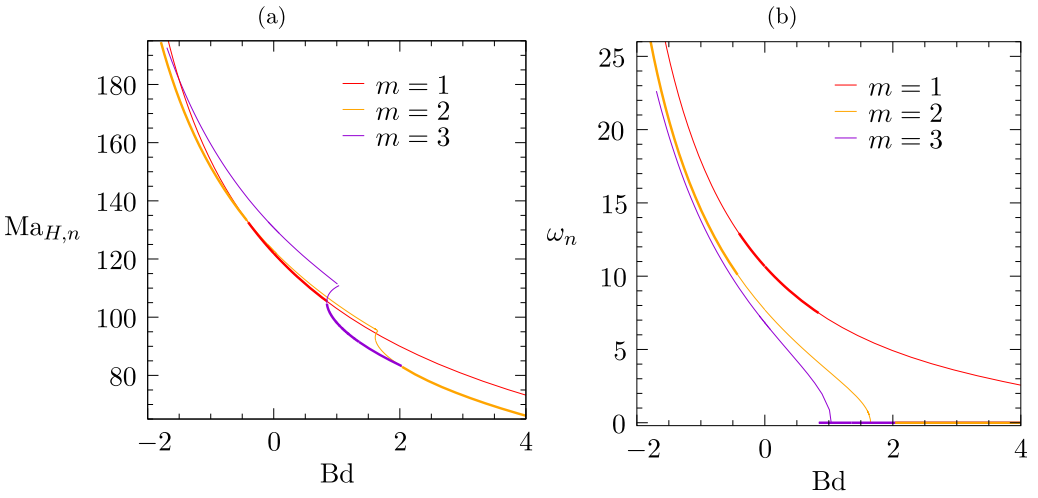

FIG. 16. The effect of buoyancy on the neutral Marangoni numbers $\mathrm{Ma}_{H,n}$ (a) and neutral oscillation frequencies ω_n (b) for $\alpha = 15^\circ$, $\mathrm{Pr} = 16.36$ and different wave numbers $m = 1$ (red), $m = 2$ (orange), and $m = 3$ (violet). Thick lines indicates critical values.

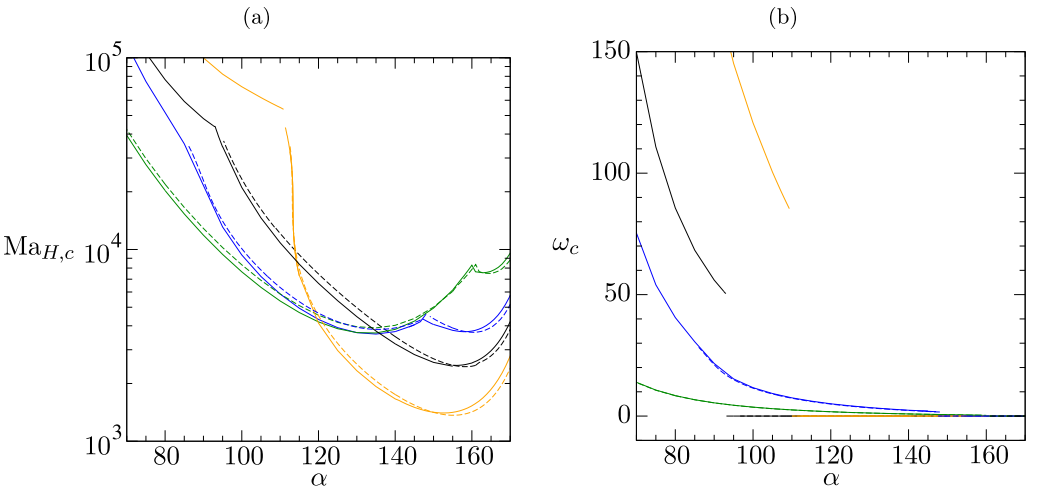

FIG. 17. Dependence of the critical Marangoni number $\mathrm{Ma}_{H,c}$ (a) and the critical oscillation frequency ω_c (b) on the contact angle α for a nonwetting droplet on a hot wall for $\mathrm{Bi} = 0.236$ (dashed line), $\mathrm{Bi} = 0.4$ (solid line) and $\mathrm{Pr} = 7$ (orange), $\mathrm{Pr} = 16.36$ (black), $\mathrm{Pr} = 28.1$ (blue), $\mathrm{Pr} = 83$ (green). The critical wave number is always $m_c = 1$.

azimuthal wave number of the oscillating mode increases from $m = 1$ to $m = 2$, as for $\alpha > 15.2^\circ$ and zero gravity [Fig. 10(b)].

It must be pointed out that for common liquids (water, ethanol, silicone oil, liquid metals), $\mathrm{Bd} \sim \mathcal{O}(1)$ would be accompanied by a nonnegligible deformation of the free-surface shape. The investigation of the effect of the shape deformation due to gravity is, however, beyond the scope of the present work. Regardless of this, the effect of strong buoyancy (large dynamic Bond number) on the steady axisymmetric flow has been studied systematically by Masoudi and Kuhlmann [25] for spherical droplets.

B. Nonwetting high-Prandtl-number droplet

As the contact angle α increases, the critical Marangoni numbers continue to rise. We did not continue the critical curves to these high values of Ma_H, because they appear unrealistic and the temperature dependence of the material parameters becomes relevant. However, for large contact angles, we find different modes of instability for which the critical Marangoni numbers decrease with α. These instabilities are considered here for a representative Biot number $\mathrm{Bi} = 0.236$ and $\mathrm{Bi} = 0.4$ to show the influence of the Biot number on the stability boundary. For contact angles larger than $\alpha \gtrsim 70^\circ$, heating from the wall and large Prandtl numbers ($\mathrm{Pr} \gtrsim 5$, depending on α) only $m = 1$ modes become critical. This is in qualitative agreement with Watanabe *et al.* [36].

We first consider the dependence of the stability boundary $\mathrm{Ma}_{H,c}$ on the contact angle. Critical curves are shown in Fig. 17(a) for several Prandtl numbers $\mathrm{Pr} > 5$ (color coded) and two Biot numbers $\mathrm{Bi} = 0.236$ and $\mathrm{Bi} = 0.4$ (distinguished by line type). Within the range of α, the Biot number has little effect on the stability boundary $\mathrm{Ma}_{H,c}$ and almost no effect on the critical oscillation frequency ω_c shown in Fig. 17(b). The critical Marangoni numbers for $\alpha = 70^\circ$ are very large. Therefore, the basic flow is relatively intense and the basic temperature field exhibits a thin boundary layer on the hot wall. Examples of the basic flow at criticality for $\mathrm{Pr} = 16.36$, $\mathrm{Bi} = 0.236$ and contact angles $\alpha = 90^\circ$ and 120° are shown in Figs. 18(a) and 18(b). Owing to the more intense flow at criticality when $\alpha = 90^\circ$ the total variation of the basic temperature field in the liquid is much less than for $\alpha = 120^\circ$ with a smaller critical Marangoni and Reynolds number. The thermal

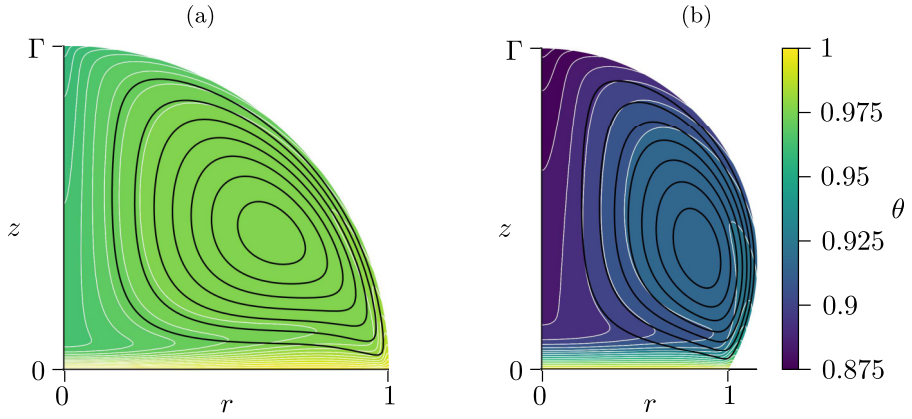

FIG. 18. Streamlines (black), isotherms (white), and temperature field (color) of the axisymmetric basic flow in nonwetting droplets on a hot wall for $\mathrm{Pr} = 16.36$, $\mathrm{Bi} = 0.236$ at the critical conditions $\alpha = 90^\circ$, $\mathrm{Ma}_H = \mathrm{Ma}_{H,c} = 52850$ (a) and $\alpha = 120^\circ$, $\mathrm{Ma}_H = \mathrm{Ma}_{H,c} = 7459$ (b).

boundary layers on the hot wall are clearly visible as well as an inverted vertical gradient of the basic temperature field just above the boundary layer.

For moderate contact angles $\alpha \sim 90^\circ$, the most dangerous mode is oscillatory and its frequency ω_c decreases if the contact angle α or the Prandtl number Pr increases [Fig. 17(b)]. Above a certain contact angle, depending on Pr, the oscillatory mode is replaced by a stationary one with the same wave number $m_c = 1$. For $\mathrm{Bi} = 0.236$ and $\mathrm{Pr} = 28.1$ and 83, the codimension-two points are located at $\alpha = 148^\circ$ and 161°, respectively.

Also the critical Marangoni number $\mathrm{Ma}_{H,c}$ decreases with α and Pr for $\alpha \sim 90^\circ$. The neutral curves of both the oscillatory and the steady modes are convex and the critical curves have minima at large contact angles, depending on Pr. For the Prandtl numbers $\mathrm{Pr} = \{7, 16.36\}$, the global minimum of $\mathrm{Ma}_{H,c}(\alpha)$ belongs to the neutral curve of the stationary mode with $\omega_c = 0$. For $\mathrm{Pr} = 28.1$ the two local minima have approximately the same Marangoni number while for $\mathrm{Pr} = 83$ the global minimum corresponds to the oscillatory mode.

The minima of the critical curves in Fig. 17 only arise for $\mathrm{Ma}_{H,c}(\alpha)$ (length scale H). The corresponding critical Marangoni number $\mathrm{Ma}_c(\alpha)$ (length scale R) decays almost exponentially with α (not shown). The decay of Ma_c, which also rules the decay of $\mathrm{Ma}_{H,c}$ for intermediate contact angles, is due to the increase of the length scale $\Gamma = H/R$ of the droplet as α increases. For very large contact angles $\alpha \to 180^\circ$, however, the aspect ratio $\Gamma \to \infty$ and $\mathrm{Ma}_{H,c}$ must diverge, since $\lim_{\alpha\to\pi} \mathrm{Ma}_c \neq 0$.

A characteristic feature of the high-Prandtl-number basic flow in a droplet exposed to a cold environment is a vertical channel of cold liquid around the axis (Fig. 18). It is created by the transport of cold liquid from a thin layer below the free surface which turns towards the wall along the axis. Since the cold temperature cannot rapidly diffuse radially due to the high Prandtl number, large radial basic-state temperature gradients are created near the axis. Figure 19 shows the typical oscillatory (a–c) and stationary (d–f) $m = 1$ modes for $\mathrm{Pr} = 16.36$ and $\mathrm{Bi} = 0.236$ associated with the two basic flows shown in Fig. 18. The velocity and temperature perturbations of the critical mode are localized near and under the apex of the droplet. This suggests that the critical mode is indeed based on the near-axis radial temperature gradients of the basic flow. The perturbation flow in Figs. 19(a) and 19(d) is approaching and leaving the apex approximately perpendicular to the isotherms of the basic flow [Figs. 18(a) and 18(b)]. By advection of basic-flow temperature, the perturbation flow creates the hot and cold temperature perturbation spots on the free surface visible in Figs. 19(c) and 19(f). In turn, the perturbations of the free surface temperature generate

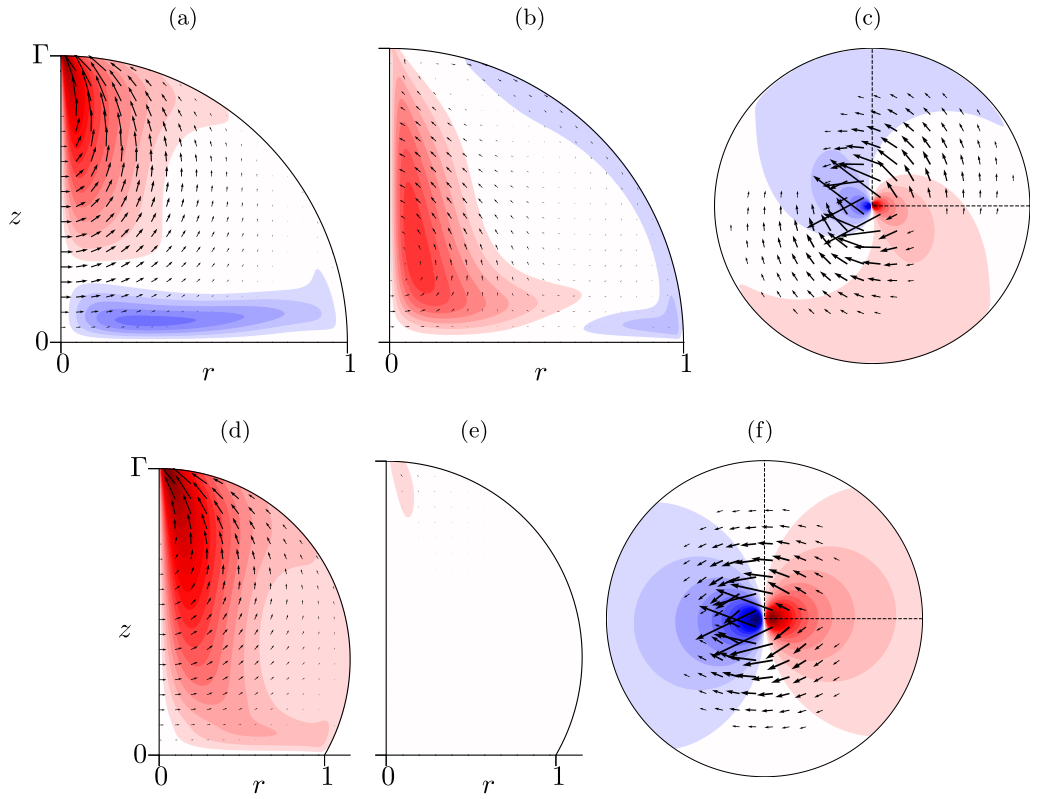

FIG. 19. Critical $m = 1$ modes for Pr = 16.36 and Bi = 0.236. (a)–(c) $\alpha = 90°$, $\mathrm{Ma}_{H,c} = 52850$, $\omega_c = 55.6$ (clockwise rotation). (d)–(f) $\alpha = 120°$, $\mathrm{Ma}_{H,c} = 7459$, $\omega_c = 0$. Panels (c) and (f) show the velocity and temperature perturbations on the free surface as seen from above. Panels (a), (b), (d), and (e) show the flow fields in vertical cross-sections indicated by dashed lines in panels (c) and (f). The corresponding basic states are shown in Fig. 18.

the perturbation flow field via the thermocapillary effect. The effect of such an $m = 1$ perturbation flow is a displacement of the total toroidal vortex and its temperature field from the axis.

The dependence of the critical Marangoni number on the Prandtl number is shown in Fig. 20(a) for $(\alpha, \mathrm{Bi}) = (140°, 0.236)$ (blue), $(\alpha, \mathrm{Bi}) = (140°, 0.4)$ (black), and $(\alpha, \mathrm{Bi}) = (120°, 0.236)$ (red). For all three parameter sets, the critical mode is oscillatory with $m = 1$ for very large Prandtl numbers and, similar as for lower contact angles, $\mathrm{Ma}_{H,c}$ saturates for very large Pr. As Pr is reduced, the oscillatory mode is replaced by a stationary one ($m = 1$). The stationary mode is strongly stabilized upon a further reduction of the Prandtl number and the critical curve $\mathrm{Ma}_{H,c}(\mathrm{Pr})$ may even turn forward (near $\mathrm{Pr} \approx 5$ for $\alpha = 120°$ and near $\mathrm{Pr} \approx 2.5$ for $\alpha = 140°$). We find the basic flows and the stationary critical modes for $\alpha = 120°$ are very similar to those for Pr = 16.36 [Figs. 18(b) and 19(d)–19(f)] all along the almost vertical critical curve. Therefore, the instability mechanism must be the same. Since thermal diffusion becomes more important as the Prandtl number is decreased, the Marangoni number must be much larger in order that the radial temperature gradients of the basic temperature field below the apex of the droplet, required for the instability, are maintained. This may explain the dramatic stabilization of the basic flow with respect to the stationary instability as Pr decreases. Finally, at even lower Prandtl numbers the stationary mode is replaced by another oscillatory mode (only shown for $\alpha = 120°$ in Fig. 20). For $\alpha = 120°$ and

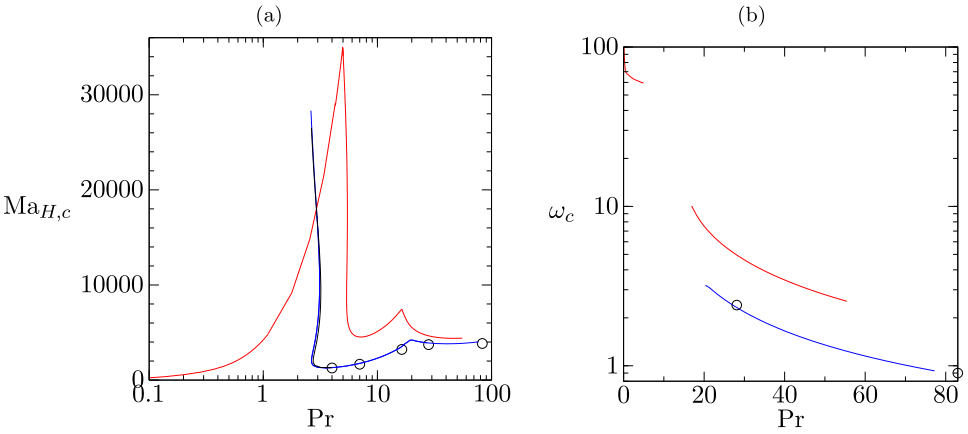

FIG. 20. Critical Marangoni number $\mathrm{Ma}_{H,c}$ (a) and critical oscillation frequency ω_c (b) as functions of the Prandtl number. Shown are curves for $(\alpha, \mathrm{Bi}) = (140^\circ, 0.4)$ (black), $(\alpha, \mathrm{Bi}) = (140^\circ, 0.236)$ (blue) and $(\alpha, \mathrm{Bi}) = (120^\circ, 0.236)$ (red). The critical azimuthal wave number is $m_c = 1$.

$\mathrm{Bi} = 0.236$ this cross-over occurs at $(\mathrm{Pr}, \mathrm{Ma}_{H,c}) = (5, 3.5 \times 10^4)$. The low Prandtl number modes are considered in more detail in the next section.

C. Nonwetting low-Prandtl-number droplet

The critical Marangoni number of the oscillatory $m = 1$ instability with $(\alpha, \mathrm{Bi}) = (120^\circ, 0.4)$ (red curves in Fig. 20) decreases rapidly with decreasing Prandtl number for $\mathrm{Pr} \lesssim 5$. Therefore, the limit of small Prandtl numbers $\mathrm{Pr} \ll 1$ is of interest. In the limit $\mathrm{Pr} \to 0$, the temperature field is dominated by thermal conduction and becomes independent of the flow. In this case, the Reynolds number instead of the Marangoni number is the appropriate similarity parameter to measure the driving force.

To approximate the low-Prandtl-number limit we consider $\mathrm{Pr} = 10^{-3}$ for which the temperature field is almost conducting as long as the Reynolds number is less than $\mathrm{Re} \lesssim 10^3$. Basic flows for $\mathrm{Pr} = 10^{-3}$ and $\mathrm{Bi} = 0.236$ are shown in Fig. 21 for $\alpha = 90^\circ$ and $\alpha = 120^\circ$. For these nonwetting droplets, the almost frozen surface temperature distribution drives a thermocapillary flow that

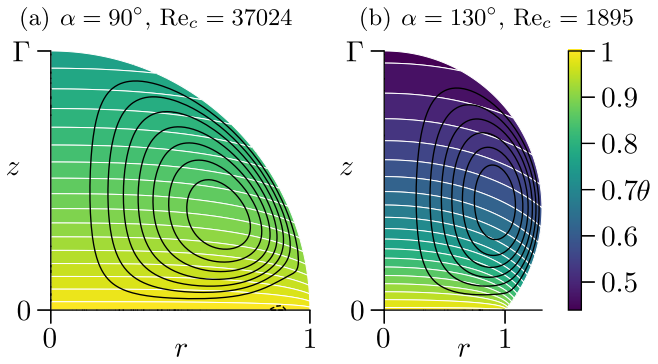

FIG. 21. Streamlines and temperature field of the axisymmetric basic flow in nonwetting droplets on a hot wall for a very low Prandtl number of $\mathrm{Pr} = 10^{-3}$, $\mathrm{Bi} = 0.236$ and contact angles $\alpha = 90^\circ$ (a) and $\alpha = 130^\circ$ (b). The basic flow is shown for critical conditions, i.e., for $\mathrm{Re}_c = 37024$ (a) and $\mathrm{Re}_c = 1895$ (b).

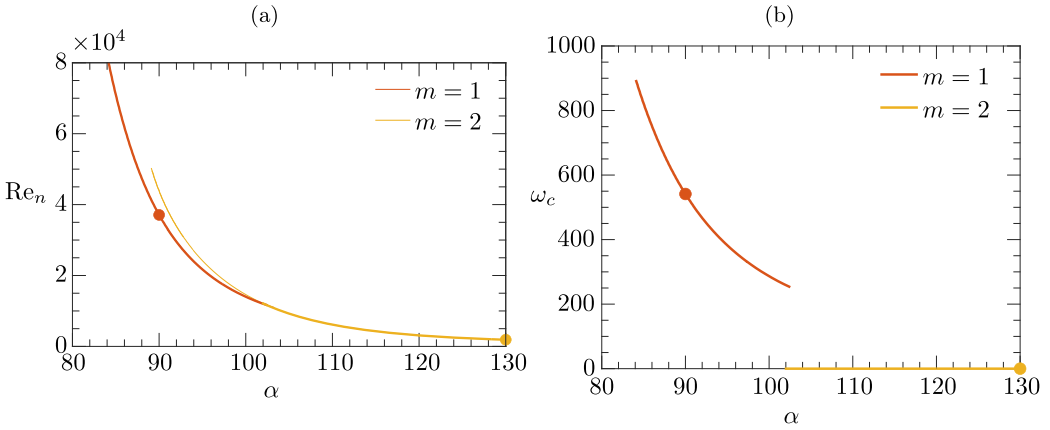

FIG. 22. Dependence of the critical Reynolds number Re_c (a) and the critical frequency ω_c on the contact angle α for droplets with $\mathrm{Pr} = 10^{-3}$, $\mathrm{Bi} = 0.236$ on a hot substrate. The dots indicate the cases shown in Fig. 21.

occupies the whole droplet. For $\alpha = 90^\circ$ [Fig. 21(a)] a small separated vortex exists on the hot wall near the contact line. It arises due to the very high Reynolds number for which the vortex core tends to approach its inertial limit and because the radially outward flow near the wall is strongly decelerated as it approaches the free surface near the contact line. This separation is similar to the separation upstream of the moving lid in the lid-driven cavity [Fig. 9(b) of Ref. [66]]. The separated region vanishes as α increases from 90° along the stability boundary. While the structure of the basic flow does not change significantly when the contact angle is varied, the critical Reynolds number reduces rapidly from $\mathrm{Re}_c = 37\,024$ for $\alpha = 90^\circ$ [Fig. 21(a)] to $\mathrm{Re}_c = 1895$ for $\alpha = 130^\circ$ [Fig. 21(b)] as the contact angle is increased. The strong reduction of Re_c is due to the combined effects caused by the increase of the droplet height H, while $\mathrm{Re} \propto R$, and the increased total variation of the surface temperature.

The dependence of the critical Reynolds number on the contact angle is shown in Fig. 22 for $\mathrm{Pr} = 10^{-3}$. It is remarkable that the oscillatory critical mode with $m = 1$ (red in Fig. 22) already seen in Fig. 20 remains critical down to such small Prandtl numbers. Only for sufficiently large contact angles does a different mode become more unstable (orange in Fig. 22). This mode is stationary and has the wave number $m = 2$. When the Prandtl number is varied for constant $\alpha = 120^\circ$ the intersection of the neutral curves for the oscillatory $m = 1$ and the stationary $m = 2$ mode arises at $(\mathrm{Pr}, \mathrm{Re}_c) = (2.1813 \times 10^{-2}, 3953)$ [circle in the inset of Fig. 23(a)]. From Fig. 23(a) it is seen that the stationary $m = 2$ mode becomes critical only at very small Prandtl numbers and remains critical for $\mathrm{Pr} \to 0$. The neutral Reynolds number as well as the oscillation frequency for the oscillatory $m = 1$ mode, however, increase strongly for $\mathrm{Pr} \lesssim 0.02$ (Fig. 23).

For $\alpha = 120^\circ$ Figs. 24(a)–24(d) compare the two modes which are neutrally stable at the codimension-two point. Shown are the surface velocity and the surface temperature fields projected in the radial (a, c) and in the axial direction (b, d). In addition, Figs. 24(e) and 24(f) show the oscillatory $m = 1$ mode for $\mathrm{Pr} = 1$ which evolves continuously from the $m = 1$ mode at the codimension-two point [Figs. 24(c) and 24(d)]. Note that for $\alpha = 120^\circ$ only the upper part of the free surface is visible in Figs. 24(b), 24(d), and 24(f)].

As a distinctive feature of the stationary $m = 2$ mode, the surface velocity is mainly directed from cold surface regions to hot surface regions [Fig. 24(a)], except for a small region near the apex. This indicates that the surface flow is not driven by the thermocapillary effect. Rather the thermocapillary forces are opposing the surface flow. Therefore, the stationary $m = 2$ perturbation flow must be created by an inertial instability of the basic flow. This interpretation is consistent with the finite limit $\mathrm{Re}_c(m = 2, \mathrm{Pr} \to 0) = 3100$. The thermocapillary stresses near the apex merely assist the

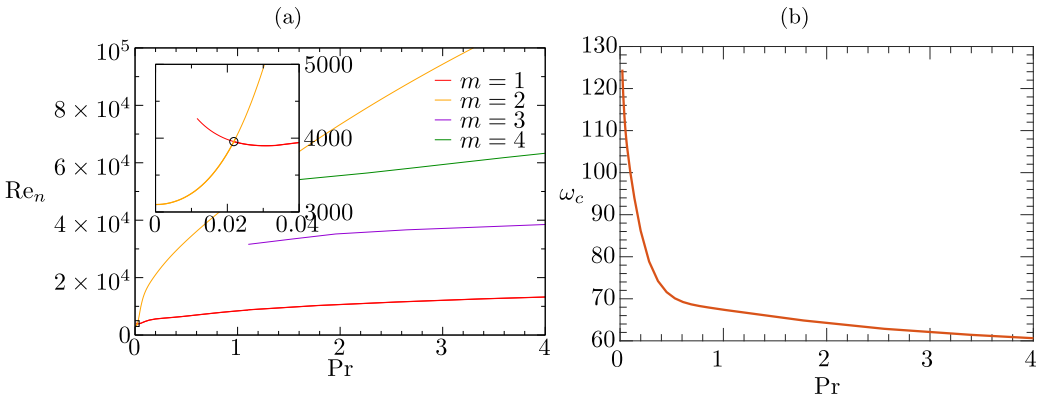

FIG. 23. Critical Reynolds number Re_c (a) and the critical frequency ω_c (b) as functions of the Prandtl number Pr for contact angle $\alpha = 120^\circ$ and $\mathrm{Bi} = 0.236$. Several other neutral Reynolds numbers are shown by thin lines in panel (a).

inertial instability. The instability resembles the stationary inertial instability in low-Prandtl-number thermocapillary liquid bridges [29,67] which is related to the instability of vortex rings caused by the self-induced strain [68]. The critical Reynolds number for the droplet on a hot wall with $\alpha = 120^\circ$ has a similar magnitude as the one in liquid bridges with the same contact angle (see Table I). In fact, the perturbation flow in the plane $z = \Gamma/2$ shown in Fig. 25(b) is very similar to the critical mode in an adiabatic thermocapillary liquid bridge for $\mathrm{Pr} = 0.02$ (see Fig. 3(a) of Wanschura *et al.* [29]). We hypothesize that the production of perturbation kinetic energy is largest near the apex of the droplet where the basic flow on the free surface is strongly decelerated and deflected axially downward. Such energy production based on flow deceleration near a hyperbolic line arises in a lid-driven cavity in which two facing walls move parallel to each other [Fig. 7(b) of Albensoeder and Kuhlmann [69]].

Figure 26 shows a three-dimensional overview of the critical Reynolds number $\mathrm{Re}_c(\alpha, \mathrm{Pr})$ computed for a hot wall and $\mathrm{Bi} = 0.236$. In contrast to the above inertial instability, the $m = 1$ oscillatory instability [Figs. 24(c)–24(e)] is the continuation of an instability from higher Prandtl numbers. At $\mathrm{Pr} = 1$, this type of instability resembles the hydrothermal waves found in thermocapillary liquid bridges [53]. These waves are characterized by strong internal temperature extrema which arise in the region of large gradients of the basic temperature field, and weak surface temperature perturbations which azimuthally advance the strong internal perturbation temperature extrema. These features are clearly seen in Figs. 25(f)–25(h). It is surprising that this mode, which is based on thermal effects, smoothly continues to be critical down to very low Prandtl numbers of the order of $\mathrm{Pr} = 0.02$, for which the instability is expected to be inertial. The very strong stabilization of the basic state with respect to this perturbation mode we find for even smaller Prandtl numbers in the limit $\mathrm{Pr} \to 0$, and the perturbation flow on the free surface which is consistent with a thermocapillary driving suggest that this mode of instability is indeed of thermal origin.

V. NONWETTING DROPLETS ON A COLD WALL

When the droplet resides on a cold instead of a hot wall, the basic flow direction on the free surface is reversed. For creeping flow, the temperature field is conducting and the shape of the streamlines and of the isotherms is identical for both a hot and a cold wall. Since flow inertia tends to shift the maximum of the free surface velocity downstream, the maximum surface velocity for a droplet on a cold wall is found closer to the contact line than in the case of a droplet on a hot wall. This is illustrated in Fig. 27 for the idealized case of $\mathrm{Pr} \to 0$ in which the temperature field

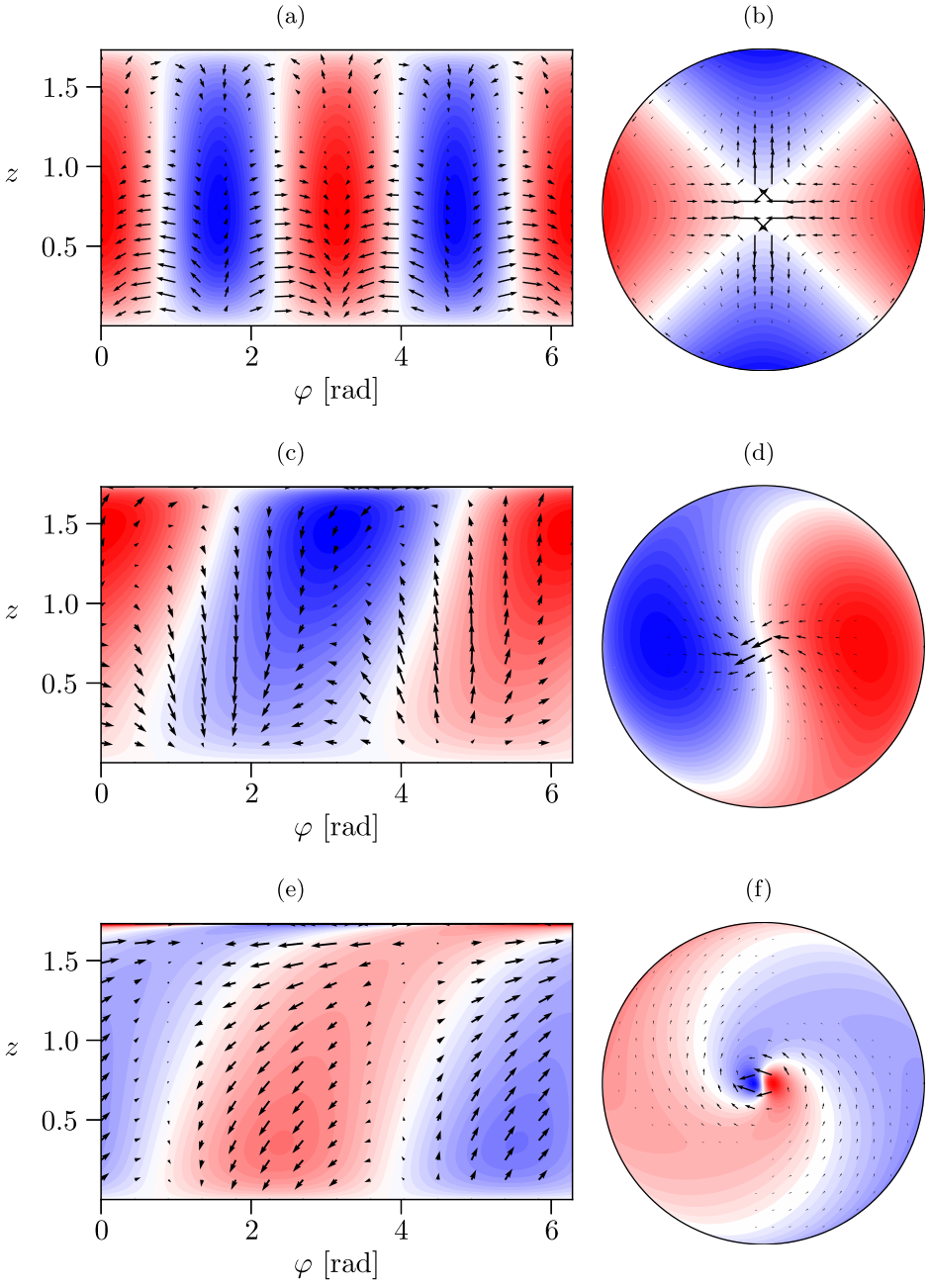

FIG. 24. Critical modes for $\alpha = 120^\circ$ and $\mathrm{Bi} = 0.236$: (a), (b) stationary mode $m = 2$ at the codimension-two point $(\mathrm{Pr}, \mathrm{Re}_c) = (2.1813 \times 10^{-2}, 3953)$, (c), (d) oscillatory $m = 1$ mode at this codimension-two point, and (e), (f) the same oscillatory $m = 1$ mode but at a much high Prandtl number for $\mathrm{Pr} = 1$ and $\mathrm{Re}_c = 8409$. The velocity and temperature on the free surface are viewed from above (right column, (b), (d), (f) and projected radially to a cylindrical surface $r = \mathrm{const.}$ (left column, (a), (c), (e). Oscillatory modes rotate clockwise.

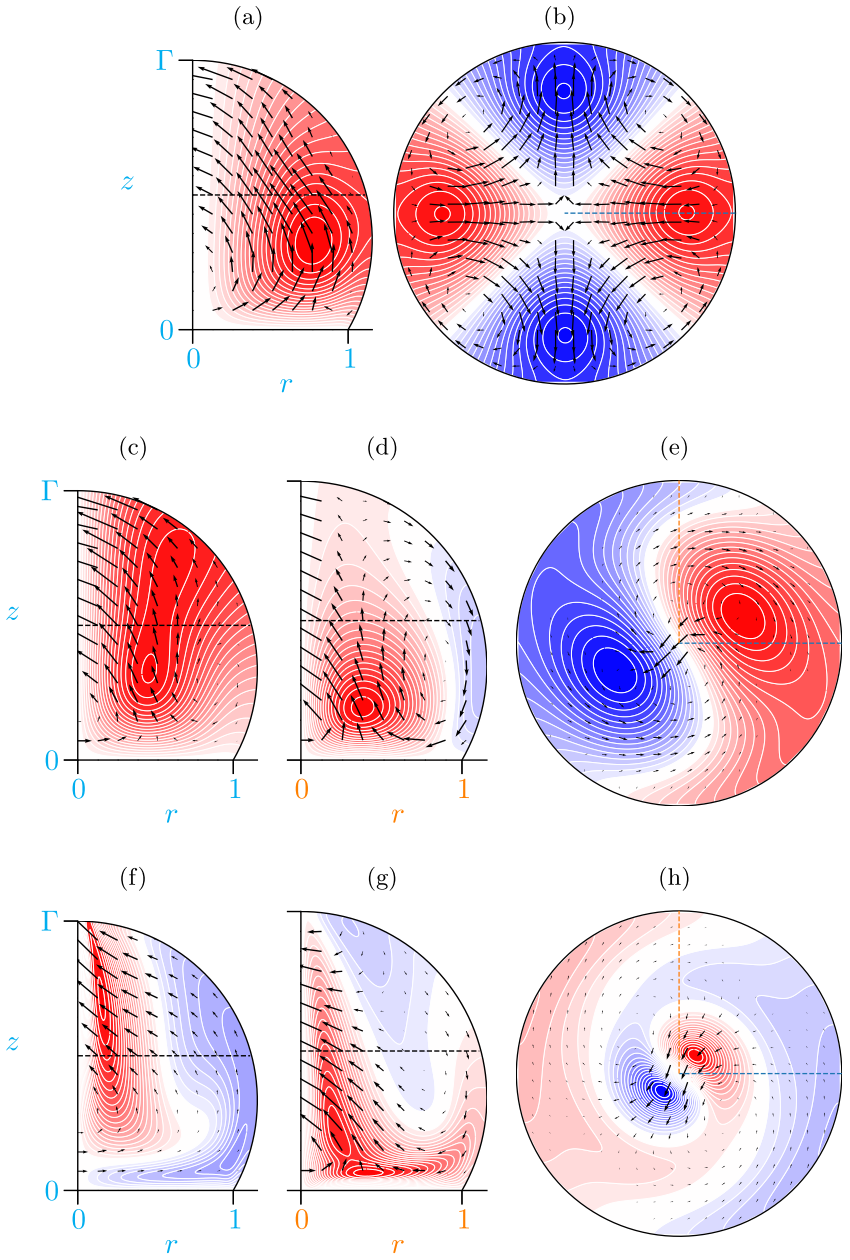

FIG. 25. Stationary mode $m = 2$ (a), (b) and oscillatory mode $m = 1$ (c)–(h) for $\alpha = 120^\circ$ both at the codimension-two point $(\mathrm{Pr}, \mathrm{Re}_c) = (2.1813 \times 10^{-2}, 3953)$. The oscillatory $m = 1$ mode on the same neutral curve but at $(\mathrm{Pr}, \mathrm{Re}_c) = (1, 8409)$ is shown in panels (f)–(h). The temperature (color) and velocity (arrows) perturbations are shown in meridional planes $\varphi = \text{const.}$ (a), (c), (d) and in the midplane $z = \Gamma/2$ (b), (e). The respective planes are indicated by the dashed lines. Oscillatory modes rotate clockwise.

is conducting. For high Prandtl numbers, this difference is even more pronounced, because of the temperature transport and the associated crowding of isotherms on the free surface.

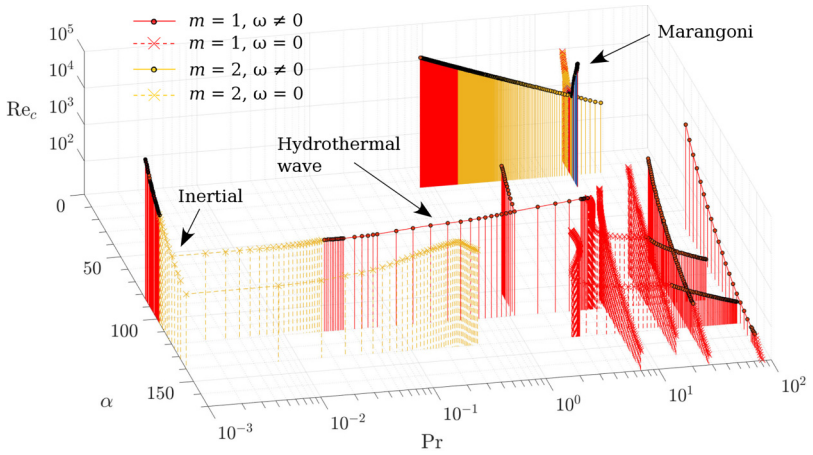

FIG. 26. Overview of the critical Reynolds number as a function of the contact angle and the Prandtl number for a hot wall and Bi = 0.236. The azimuthal wave number is coded by color: $m = 0$ (blue), $m = 1$ (red), $m = 2$ (orange), $m = 3$ (violet), $m = 4$ (green), $m = 5$ (cyan), $m = 6$ (maroon). Filled circles with black edges connected by full lines indicate oscillating modes $\omega_c \neq 0$, while crosses connected by dashed lines indicate steady modes $\omega_c = 0$.

A. Low-Prandtl-number instability

For cooling from the wall the fluid temperature increases towards the free surface. Therefore, the Pearson mechanism tends to suppress any temperature perturbations on the free surface and the critical Reynolds numbers are expected to be large, in particular for shallow droplets. For shallow droplets, inertial instabilities are very unlikely because, in addition to the stabilizing temperature gradient normal to the interface, the flow velocities are small.

To demonstrate the inertial instability for large-contact-angle droplets, unperturbed by thermal effects, we consider the idealized case of $\mathrm{Pr} \to 0$, which may approximate the behavior in liquid metals. The critical Reynolds number as a function of the contact angle is shown in Fig. 28. Throughout the range of α shown the instability is stationary with critical wave number $m = 2$. Representative basic flows at criticality are shown in Fig. 29 for $\alpha = 90^\circ$ (a), $\alpha = 120^\circ$ (b), and

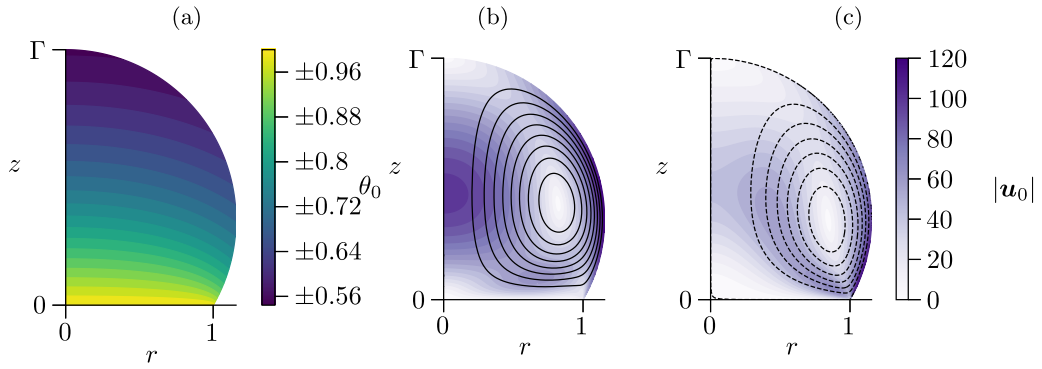

FIG. 27. Basic state for $\mathrm{Pr} = 0$, $\alpha = 120^\circ$ and $\mathrm{Re} = 2000$. Shown are (a) the isotherms of the (conducting) basic temperature field, (b) streamlines for a droplet on a hot wall (counterclockwise rotation), and (c) those for a droplet on a cold wall (clockwise rotation). The gray scale in panels (b), (c) indicates the velocity magnitude. Note the contours of the conducting temperature field are identical but θ_0 has an opposite sign for (b), (c).

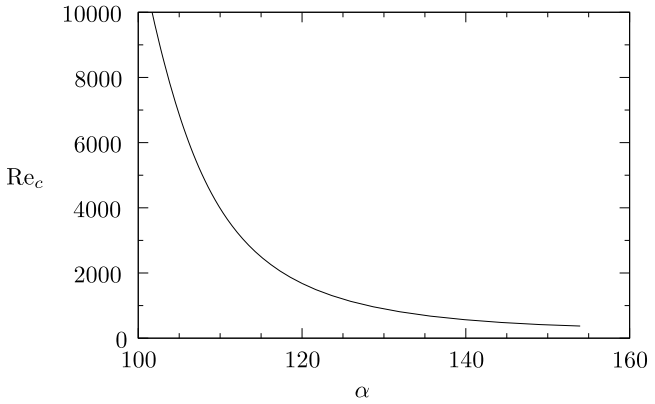

FIG. 28. Critical Reynolds number as function of the contact angle α for a cold substrate and $\mathrm{Pr} \to 0$. The critical mode with wave number $m_c = 2$ is stationary.

$\alpha = 140^\circ$ (c). For large contact angles [Fig. 29(c)] the droplet is tall and it reaches farther into the hot ambient than the droplets with smaller contact angles. Therefore, the total variation of the surface temperature is larger (for the same effect and a hot wall, see Fig. 21) and the vortex reaches closer to the apex than for smaller contact angles. For $\alpha = 100^\circ$ [Fig. 29(a)], however, the basic vortex is confined to the region near the contact line such that the flow separates from the wall. Since the inertial instability relies on the strain field of the vortex, the decrease of the critical Reynolds number with α is due to the larger strain which the basic vortex provides for $\alpha = 140^\circ$ when it is stretched axially as compared to $\alpha = 100^\circ$.

The stationary critical modes for all three contact angles are shown in Fig. 30. In the horizontal cross section at $z = \Gamma/2$ the critical modes for $\alpha = 120^\circ$ and 140° [Figs. 30(b) and 30(c)] appear as four vortices, very similar as the low-Prandtl-number critical mode in thermocapillary liquid bridges [29]. From Figs. 30(h) and 30(i) is seen that the axes of the perturbation vortices are tilted towards the coordinate axis in the upper part of the droplet. The velocity field of the critical mode being strongest near the center of the basic toroidal vortex [see Figs. 30(e) and 30(f)] suggests a mechanism similar to the vortex ring instability [68], i.e., the elliptic instability mechanism [70–72]. The critical mode for $\alpha = 100^\circ$ which becomes critical at much higher Reynolds numbers differs from those for $\alpha = 120^\circ$ and 140°. From Figs. 30(d) and 30(g) the axes of the perturbation vortices are now almost parallel to the wall and located in the upper part of the droplet where the basic flow is weak.

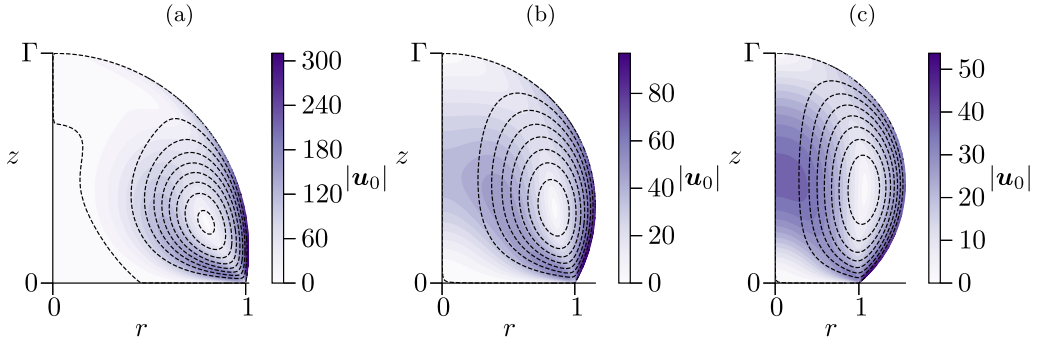

FIG. 29. Streamlines and absolute velocity of the basic flow in a droplet on a cold substrate for $\mathrm{Pr} = 0$ and $\alpha = 100^\circ$, $\mathrm{Re}_c = 12\,062$ (a), $\alpha = 120^\circ$, $\mathrm{Re}_c = 1680$ (b), and $\alpha = 140^\circ$, $\mathrm{Re}_c = 564.2$ (c).

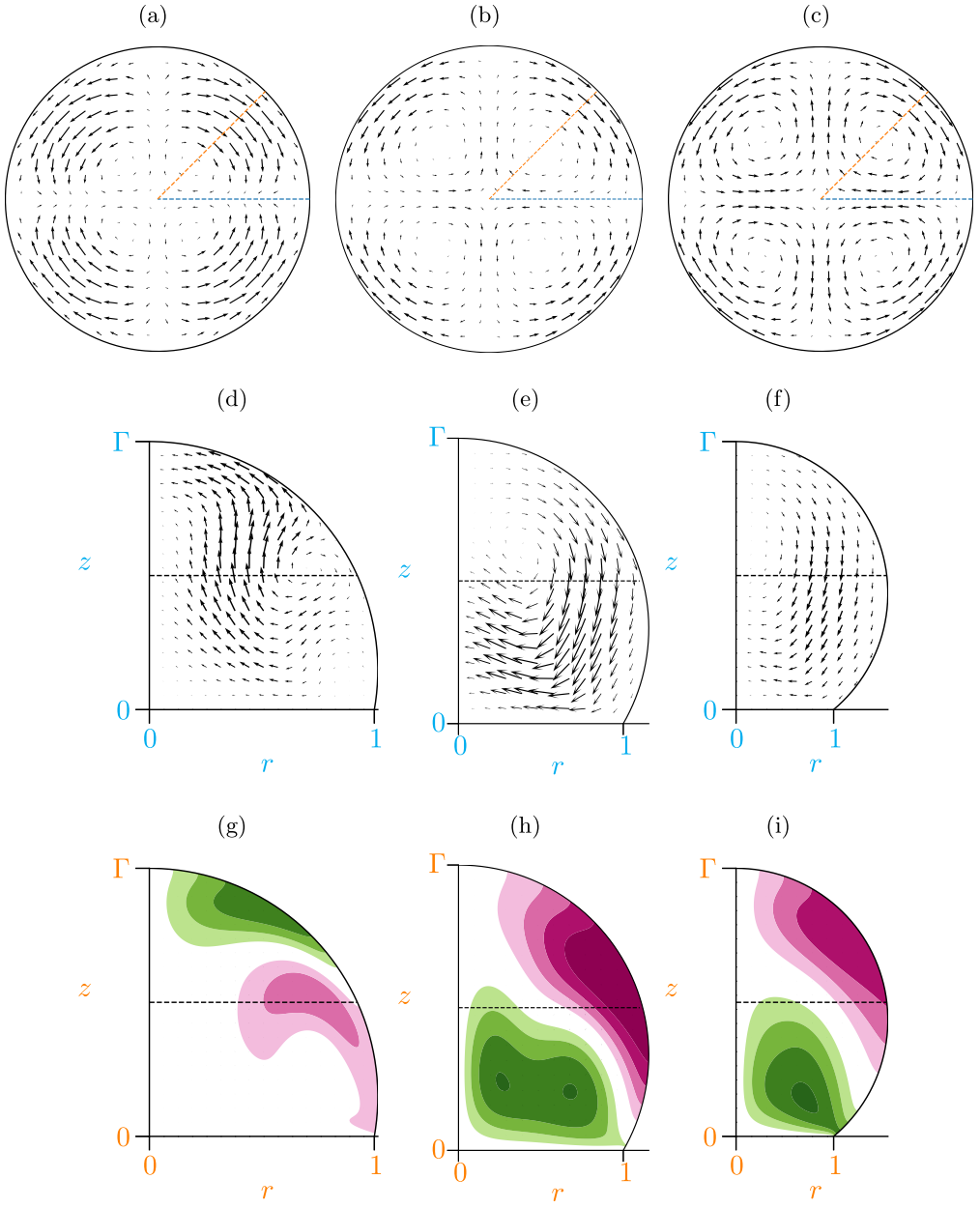

FIG. 30. Critical modes for a droplet with Pr = 0 on a cold substrate and $\alpha = 100°$, Re = 12 062 (a), (d), (g), $\alpha = 120°$, Re = 1680 (b), (e), (h), $\alpha = 140°$, Re = 564.2 (c), (f), (i). All modes are stationary with $m_c = 2$. The top row (a)–(c) shows the perturbation velocity in the midplane $z = \Gamma/2$, and the middle (d)–(f) and the bottom row (g)–(i) show the corresponding critical modes in meridional cuts indicated by the blue and orange dashed lines in panels (a)–(c), respectively. The green and pink colors in the bottom row indicate the positive and negative azimuthal velocities, respectively.

The low-Prandtl-number instability for large contact angles is qualitatively similar for droplets on a cold wall and those on a hot wall [Figs. 21(b) and 24(a), 24(b)]. Also, the dependence of the critical Reynolds number on α for the stationary $m = 2$ modes are similar in both cases [compare Figs. 22(a) and 28]. This underlines the inertial mechanism based on the straining of the basic vortex

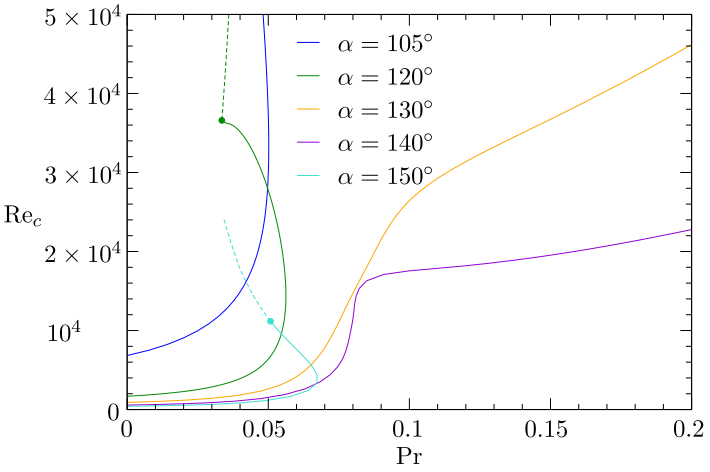

FIG. 31. Neutral curves $\mathrm{Re}_n(\mathrm{Pr})$ for $m = 2$ and a droplet on a cold wall for different contact angles (coded by color). The critical wave number is $m_c = 2$, throughout. Full lines indicate stationary modes. Dashed lines mark oscillatory modes with frequencies $\omega_n \sim \mathcal{O}(10)$.

which is elongated in the wall-normal direction for large contact angles regardless of the wall being hot or cold.

The dependence of the critical Reynolds number on the Prandtl number is shown in Fig. 31 for the inertial instability. As Pr increases from zero, the basic flow is strongly stabilized, depending on the contact angle. The reason is the critical inertial mode generates a temperature perturbation which creates a thermocapillary stress opposing the perturbation flow on the free surface. Since the temperature perturbations become stronger with increasing Prandtl number, the self-suppression is enhanced with Pr. This effect is similar as in liquid bridges [73] and has also been observed for droplets on a hot wall (Sec. IV C) for the stationary $m = 2$ mode. In Fig. 31 the neutral curves $\mathrm{Re}_n(\mathrm{Pr})$ for $\alpha = 120°$ and $\alpha = 150°$ turn backward and may intersect with other neutral modes. Such codimension-two points are shown by the dots in Fig. 31 for $\alpha = 120°$ and $\alpha = 150°$, where the stationary branch intersects with the neutral curve of an oscillatory $m = 2$ mode. For a millimeter-sized droplet of mercury or galinstan (for the thermophysical properties see

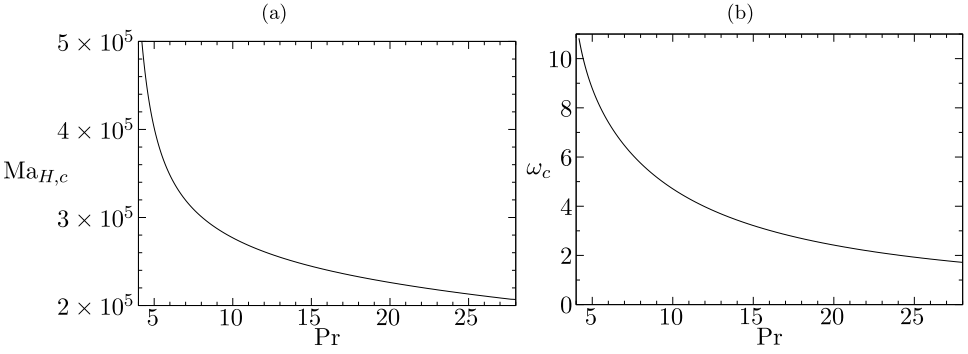

FIG. 32. Dependence of the critical Marangoni number $\mathrm{Ma}_{H,c}$ (a) and of the critical frequency ω_c (b) on the Prandtl number Pr for a cold substrate, $m_c = 1$, $\alpha = 140°$, and $\mathrm{Bi} = 0.4$

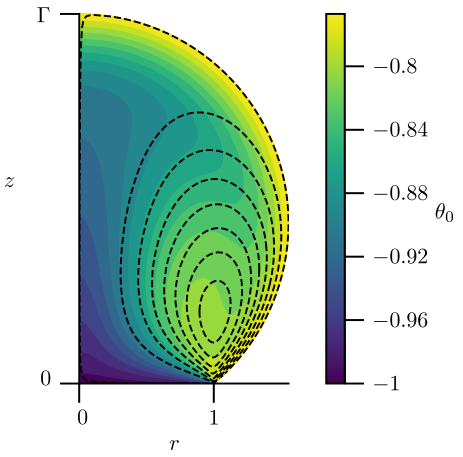

FIG. 33. Marginally stable basic state (streamlines and temperature field) for a droplet on a cold wall, $\alpha = 140°$, Pr = 28.1, Bi = 0.4, and $\mathrm{Ma}_{H,c} = 206889$.

Refs. [74–76]), the Reynolds number of the codimension-two point $\mathrm{Re}_n \sim \mathcal{O}(10^4)$ corresponds to $\Delta T \sim \mathcal{O}(10\ \mathrm{K})$. For all contact angles the critical Reynolds number exceeds 10^4 when $\mathrm{Pr} \gtrsim 0.08$.

B. High-Prandtl-number instability

The basic flow beyond $\mathrm{Pr} > 0.2$ is very stable until, for $\mathrm{Pr} \gtrsim 1$, the inertial instability is replaced by a hydrothermal wave instability. The critical Marangoni number $\mathrm{Ma}_{H,c}$ as a function of the Prandtl number is shown in Fig. 32 for $\alpha = 140°$ and Bi = 0.4. The behavior for Bi = 0.236 is similar (not shown). The critical Marangoni numbers $\mathrm{Ma}_{H,c}$ are significantly larger than the ones

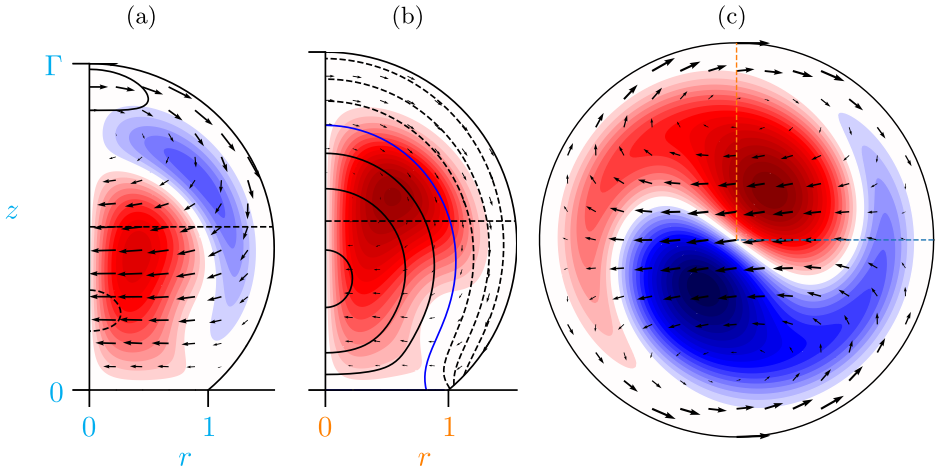

FIG. 34. Critical velocity (arrows) and temperature field (color) of a $m_c = 1$ hydrothermal wave traveling azimuthally [clockwise in panel (c)] with $\omega_c = 1.71$ in a droplet on a cold wall. The parameters are $\alpha = 140°$, Pr = 28.1, Bi = 0.4, and $\mathrm{Ma}_{H,c} = 206\,889$. The critical mode is displayed in two orthogonal planes of $\varphi =$ const. (a), (b) and in the midplane $z = \Gamma/2$ (c). The planes in panels (a) and (b) are indicated, respectively, by the blue and orange dashed lines in panel (c). Contours of equal azimuthal velocity are shown in panel (a), (b) as full ($v > 0$) and dashed curves $v < 0$ [blue curve in panel (b): $v = 0$].

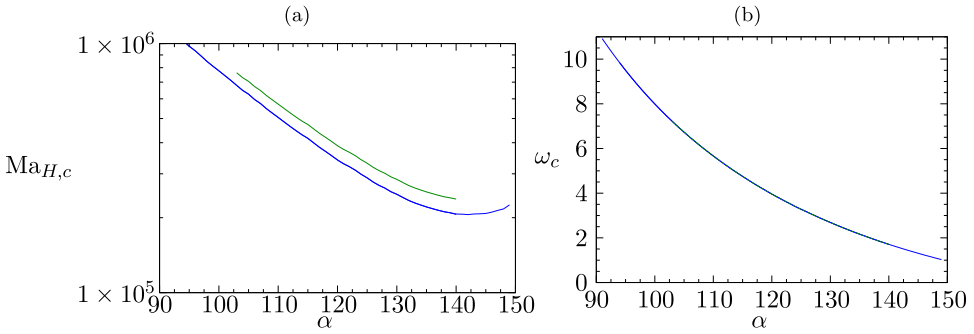

FIG. 35. Critical Marangoni number $\mathrm{Ma}_{H,c}$ (a) and frequency ω_c (b) as functions of the contact angle α for a cold substrate, $m_c = 1$ and $\mathrm{Pr} = 28.1$. The Biot numbers are $\mathrm{Bi} = 0.4$ (blue) and $\mathrm{Bi} = 0.236$ (green).

for a droplet on a hot wall. Throughout the range of Prandtl numbers shown the critical mode is oscillatory with wave number $m_c = 1$. For a given contact angle $\alpha \geqslant 90^\circ$ the critical Marangoni number decreases with increasing Prandtl number and might eventually saturate at a nonzero value for $\mathrm{Pr} \to \infty$.

As an example we consider $\alpha = 140^\circ$, $\mathrm{Pr} = 28.1$, $\mathrm{Bi} = 0.4$ with $\mathrm{Ma}_{H,c} = 206\,889$. The basic flow on the stability boundary is shown in Fig. 33. Owing to the high Marangoni number, the internal isotherms are almost parallel to the streamlines of the basic toroidal vortex flow. The high-Prandtl-number instability is based on the associated large radial temperature gradients of the plumelike cold finger on the axis which originates from the cold wall. The critical mode shown in Fig. 34 draws its energy from these radial temperature gradients by advecting basic state temperature. It is seen that the perturbation velocity field is directed across the axis and arises primarily in the lower half of the droplet [Fig. 34(a)]. The advection of the basic state temperature thus creates the strong internal temperature extrema shown in color in Fig. 34. The perturbation flow itself is driven primarily in the azimuthal direction by surface tension gradients created by comparatively weak surface temperature variations which are ultimately created by thermal conduction from the internal perturbation temperature extrema. These properties of the basic and the perturbation flow indicate the instability mode is a hydrothermal wave [28,29].

The dependence of the critical Marangoni number on the contact angle α is displayed in Fig. 35(a). The dependence is qualitatively similar to the one for droplets on a hot wall [Fig. 17(a)], although the structures of the critical modes in Figs. 19 and 34 differ considerably. $\mathrm{Ma}_{H,c}$ decreases almost exponentially with $\alpha \in [90^\circ, 120^\circ]$ and reaches a minimum at $\alpha = 140^\circ$ for $\mathrm{Bi} = 0.4$ and $\mathrm{Pr} = 28.1$. The critical frequency ω_c [Fig. 17(b)] varies moderately with α, but is almost independent of the Biot number within the considered range of α for $\mathrm{Pr} = 28.1$: The curve $\omega_c(\alpha)$ for $\mathrm{Bi} = 0.236$ is indistinguishable from the one for $\mathrm{Bi} = 0.4$ on the scale shown.

VI. SUMMARY AND CONCLUSIONS

The linear stability of the steady axisymmetric flow in droplets with a spherical cap attached to a wall hotter or colder than the environment has been computed numerically. To enable a quasicontinuous variation of the contact angle and the Prandtl number the heat transfer from the free surface has been idealized using Newton's law of cooling.

For shallow droplets of 1 cSt silicone oil on a hot wall the axisymmetric flow is not unique. We find a similar bifurcation structure as for an infinitely extended plane layer heated from the wall [57,58]. Steady concentric convection rolls come into existence at the apex of the shallow droplet via a transcritical bifurcation. Contrary to plane layers, the bifurcation in the droplet is weakly

perturbed by the global thermocapillary flow driven over the whole free surface. For Marangoni numbers slightly above the imperfect bifurcation point, the solution connected with the subcritical global thermocapillary flow becomes unstable by an axisymmetry-breaking three-dimensional flow. For larger contact angles the steady concentric Marangoni rolls are suppressed by the global thermocapillary circulation and the Marangoni instability becomes nonaxisymmetric with stationary roll-like solutions which are azimuthally modulated with wave numbers $m = 2$ and $m = 4$. For even larger contact angles spiral waves appear which are also destabilized by the classical Marangoni mechanism. Common to all wetting droplets for 1 cSt silicone oil on a hot wall is a very dense gathering of the neutral stability boundaries for axi- and nonaxisymmetric modes. This property may explain the rapid succession of different flow patterns as the contact angle or the Marangoni number changes [see, e.g., Ref. [35]]. Some of the nonaxisymmetric flow patterns observed by Shi *et al.* [35] for Marangoni numbers below the present linear stability threshold may have come into existence via a transcritical bifurcation, similar to the steady concentric convection rolls.

Depending on the Prandtl number and the contact angle also instabilities have been found which are created by inertial or hydrothermal-wave mechanisms, or combinations thereof. These inertial and hydrothermal-wave instabilities arise for nonwetting droplets on a hot wall, a case only sparsely reported in the literature. The velocity fields of the critical hydrothermal waves are of interest, because the nonlinear azimuthally propagating waves emerging from the instability are believed to be responsible [see, e.g., Ref. [77]] for the particle accumulation structures observed experimentally in droplets pending from a hot wall [26,36].

A difficulty often faced by both experiments and single fluid numerical analyses is an uncertainty regarding the ambient conditions. Watanabe *et al.* [36] measured the onset of oscillations in thermocapillary buoyant droplets pending from a hot wall when a cold wall was placed in immediate vicinity of the apex of the droplet, almost making contact. They expressed the critical conditions in terms of the temperature difference between both walls. For $\Gamma = 1$ their Fig. 3 yields $\Delta T_c^{\mathrm{exp}} = 27$ K for $\mathrm{Pr} = 28.1$. Assuming the droplet shape can well be approximated by a half sphere of radius R the critical Marangoni number becomes $\mathrm{Ma}_c^{\mathrm{exp}} = 2.33 \times 10^4$. The present result for $\Gamma = 1$, $\mathrm{Pr} = 28.1$ and $\mathrm{Bi} = 0.4$ is $\mathrm{Ma}_c = 7.55 \times 10^4$. The discrepancy is mainly due to the different definitions of the characteristic temperature difference. A better measure for the characteristic temperature would be $\Delta T_{\mathrm{apex}} := |T_{\mathrm{apex}} - T_{\mathrm{wall}}|$. This temperature difference is proportional to the total variation of the surface tension along the free surface, similar as in thermocapillary liquid bridges. Based on the nondimensional critical apex temperature $\vartheta_{\mathrm{apex},c} = 0.9428$ for the case considered we obtain $\mathrm{Ma}_c^{\mathrm{apex}} = |\vartheta_{\mathrm{apex},c} - 1|\mathrm{Ma}_c = 7051$. Similarly, ΔT_{apex} in the experiment of Ref. [36] most likely was much less than 27 K, because the flow in the lubrication film between droplet and cold wall prevents the apex of the droplet to attain the cold wall temperature [78,79]. This is confirmed by the IR temperature measurement in figure 6(b) of Ref. [36] which suggests that ΔT_{apex} is at least 50% less than the nominal value of ΔT, which leads to the estimate $\mathrm{Ma}_c^{\mathrm{apex,exp}} \lesssim 1.2 \times 10^4$. This shows that the critical conditions based on the ΔT_{apex} are indeed comparable, notwithstanding the remaining differences caused by the different gravity levels, differences in shape and in the temperature distribution along the surface of the droplet. In fact, the critical wave number is $m_c = 1$ in both cases.

We did not find instabilities corresponding to the convective rolls and Bénard-Marangoni cells near the contact line, which were observed in evaporating droplets experimentally [20] and numerically by three-dimensional time-dependent simulations [22]. It seems natural to attribute these flow patterns to the substantial changes in the thermal and solutal boundary conditions at the free surface due to the evaporation and the associated local cooling effect. The comparison between our results and the linear stability analysis of Karapetsas *et al.* [39], however, reveals that the thermal boundary condition at the free surface does not have a severe effect on the qualitative structure of the most dangerous modes. The time-dependent three-dimensional simulations of Kumar, Medale and Brutin [80] show that even for evaporating shallow droplets the Marangoni instability is indeed triggered near the center of the droplet, as predicted by our linear stability analysis. Soon after these initial cells appear, they rapidly spread through the rest of the droplet, a feature which cannot be

captured by our linear analysis. These cells are then sustained even relatively close to the contact line, most likely due to the large local evaporative cooling.

Nonwetting droplets on a cold wall in a hot atmosphere were considered as well. At low Prandtl numbers, an inertial instability of the concentric vortex flow exists, similar to the one in thermocapillary liquid bridges [29]. These instabilities are suppressed, however, as the droplet becomes more shallow, because of the stabilizing Marangoni effect. For a high-Prandtl-number droplet on a cold wall, we find a hydrothermal wave instability, but the critical Marangoni numbers are orders of magnitude larger than those for a hot wall.

The present results on the flow instability of nonvolatile thermocapillary droplets may serve as reference data for numerical investigations of extended models which may take into account solutal effects [81,82], the inhomogeneous cooling of the interface by the latent heat due to evaporation [39,83–88], buoyancy forces [24,37], including deviations from a spherical droplet shape [89], the heat, mass, and momentum transport in the ambient atmosphere [53,90], and the thermal properties of the wall [20,91,92].

ACKNOWLEDGMENTS

L.B. gratefully acknowledges partial financial support of this work by AIC Androsch International Management Consulting GmbH. The authors also thank Pierre-Emmanuel des Boscs for countless consultations on the technical aspect of this work, for sharing his numerical package, and for extensive help with setting up the computations.

APPENDIX A: RADIATION HEAT TRANSFER AT THE FREE SURFACE

To compare the present linear stability results with the numerical simulations of Shi *et al.* [35] in Fig. 6 we consider a radiation heat flux between the free surface of the droplet and the ambient according to the Stefan-Boltzmann law

$$\tilde{q}_r = \epsilon\sigma_r\left(T^4 - T_a^4\right), \tag{A1}$$

where ϵ is the emissivity of the free surface, σ_r is the Stefan–Boltzmann constant, and T_a is the absolute ambient temperature. In our scaling the dimensionless form of radiation heat flux reads

$$q_\mathrm{r} = \mathrm{Bi}_\mathrm{r}\frac{\Pi}{\mathrm{Re}}\left[\left(\theta\frac{\mathrm{Re}}{\Pi}+1\right)^4 - 1\right], \tag{A2}$$

where $\mathrm{Bi}_\mathrm{r} = \epsilon\sigma_r T_a^3 R/k$ and $\Pi = \gamma T_a R/(\rho\nu^2)$. While the radiation is emitted and absorbed in the bulk of the fluid, we take the limit of large absorption coefficient of the fluid. In this approximation, any radiation from the droplet is (for moderate temperature variations) emitted or absorbed within an infinitely thin layer of fluid beneath the free surface.

The linear combination of Newton's law and Stefan-Boltzmann's law leads to

$$\boldsymbol{n}\cdot\nabla\theta_0 = -\left\{\mathrm{Bi} + \mathrm{Bi}_\mathrm{r}\frac{\Pi}{\mathrm{Re}}\left[\left(\theta_0\frac{\mathrm{Re}}{\Pi}+1\right)^4 - 1\right]\right\}\theta_0, \tag{A3}$$

which is used as the thermal boundary condition for basic flow instead of (4g) whenever radiation is taken into account. The expression in the curly brackets represents the effective Biot number Bi_eff used by Shi *et al.* [35]. In the linear stability analysis the linearized version of Eq. (A3),

$$\boldsymbol{n}\cdot\nabla\theta' = -\{\mathrm{Bi} + 4\mathrm{Bi}_\mathrm{r}\}\theta', \tag{A4}$$

is implemented to compute the perturbation flow.

The dimensional parameters used by Shi *et al.* [35] are $h_c = 8.08\,\mathrm{W/(m^2K)}$, $\epsilon = 0.91$, $T_a = 298.15$ K, $R = 2.5\times10^{-3}$m. The remaining parameters are provided in Table IV. For these condi-

TABLE IV. Thermophysical parameters of 1 cSt silicone oil. The data are the same as in Ref. [35].

Parameter	Symbol	Value
Thermal conductivity	k	0.1 W/(m K)
Temperature coefficient of surface tension	γ	7.55×10^{-5} N/(m K)
Density	ρ	818 kg/m^3
Kinematic viscosity	ν	10^{-6} m^2/s
Thermal diffusivity	κ	6.112×10^{-8} m^2/s

tions, we obtain $\mathrm{Bi} = 0.202$, $\mathrm{Bi_r} = 0.0342$, and $\Pi = 68797$ and the linear stability analysis yields the critical curve shown in Fig. 6. The critical Marangoni numbers compare favorably with the numerical results of Shi *et al.* [35] (reproduced from their Fig. 4 as triangles in Fig. 6).

APPENDIX B: THE METHOD OF NITSCHE TO IMPOSE A NO-PENETRATION CONDITION ON THE FREE SURFACE

The weak formulation of the Navier-Stokes subsystem (3a) and (3b) reads: Find $\boldsymbol{u}_h$, p_h such that

$$([\partial_t + \boldsymbol{u}_h \cdot \nabla]\boldsymbol{u}_h, \boldsymbol{v}) - (p_h, \nabla \cdot \boldsymbol{v}) + (\boldsymbol{s}_h, \nabla \boldsymbol{v}) + \langle \boldsymbol{n} \cdot (p_h \mathbf{I} - \boldsymbol{s}_h), \boldsymbol{v} \rangle = 0 \quad \forall \boldsymbol{v} \in \mathbb{P}_2^2, \tag{B1a}$$

$$-(\nabla \cdot \boldsymbol{u}_h, q) = 0 \quad \forall q \in \mathbb{P}_1, \tag{B1b}$$

where the subscript $_h$ indicates the interpolation of the nodal values with the given basis functions, $\boldsymbol{n}$ is a boundary normal, $\boldsymbol{v}$ and q are test functions, $\boldsymbol{s}_h = \nabla \boldsymbol{u}_h + \nabla \boldsymbol{u}_h^{\mathrm{T}}$ and the inner products are

$$(\boldsymbol{a}, \boldsymbol{b}) = \int_\Omega \boldsymbol{a} : \boldsymbol{b} \mathrm{d}\Omega, \quad \langle \boldsymbol{a}, \boldsymbol{b} \rangle = \int_{\partial\Omega} \boldsymbol{a} \cdot \boldsymbol{b} \mathrm{d}S,$$

where Ω is the domain and $\partial\Omega$ the domain boundary. On the wall $z = 0$ and on the axis $r = 0$, the boundary integral vanishes due to Dirichlet boundary conditions imposed in a strong form and homogeneous Neumann boundary conditions.

At the free surface, independent boundary conditions in the normal and tangential directions are imposed, which do not coincide with coordinate lines. Thus, the stress on the boundary and the test function $\boldsymbol{v}$ are decomposed into the normal and the two orthogonal tangential directions by the projection operators $\boldsymbol{nn}$, $\boldsymbol{tt}$ and $\boldsymbol{e}_\varphi \boldsymbol{e}_\varphi$ (dyadic products) to obtain

$$\langle p_h \boldsymbol{n} - \boldsymbol{n} \cdot \boldsymbol{s}_h, \boldsymbol{v} \rangle = \langle p_h \boldsymbol{n} - \boldsymbol{n} \cdot \boldsymbol{s}_h \cdot \boldsymbol{nn}, \boldsymbol{v} \cdot \boldsymbol{nn} \rangle + \langle \boldsymbol{n} \cdot \boldsymbol{s}_h \cdot \boldsymbol{tt}, \boldsymbol{v} \cdot \boldsymbol{tt} \rangle + \langle \boldsymbol{n} \cdot \boldsymbol{s}_h \cdot \boldsymbol{e}_\varphi \boldsymbol{e}_\varphi, \boldsymbol{v} \cdot \boldsymbol{e}_\varphi \boldsymbol{e}_\varphi \rangle. \tag{B2}$$

The tangential stresses on the boundary can be substituted by the thermocapillary stresses from Eqs. (4d) and (4e). The normal boundary stress tensor is treated with the method of Nitsche [46] to enforce the no-penetration condition on the free surface. In Nitsche's method, additional terms are added to the left-hand side of the weak formulation (B1) to penalize the deviation from the prescribed Dirichlet boundary condition (in our case the no-penetration condition). The penalty term

$$\frac{C}{h_e} \langle \boldsymbol{u}_h \cdot \boldsymbol{nn}, \boldsymbol{v} \cdot \boldsymbol{nn} \rangle,$$

where $C = 60$ is a penalization constant and h_e is the circumradius of the respective finite element, is added to the left-hand side of Eq. (B1a). Furthermore, a stabilization term

$$\langle q\boldsymbol{n} - \boldsymbol{n} \cdot (\nabla \boldsymbol{v} + \nabla \boldsymbol{v}^{\mathrm{T}}) \cdot \boldsymbol{nn}, \boldsymbol{u}_h \cdot \boldsymbol{nn} \rangle,$$

which is a symmetric counterpart of the normal boundary stress term, is added to the left-hand side of Eq. (B1b).

APPENDIX C: SINGULARITY OF THE PERTURBATION EQUATIONS ON THE AXIS FOR $m = 1$

The equations for $\mu\hat{u}$ and $\mu\hat{v}$ in the system of perturbation equations (12) contain, respectively, the following terms from the divergence of the viscous stress tensor

$$-\frac{m^2+2}{r^2}\hat{u} - \frac{3\mathrm{i}m}{r^2}\hat{v} \quad \text{and} \quad -\frac{2m^2+1}{r^2}\hat{v} + \frac{3\mathrm{i}m}{r^2}\hat{u},$$

which are proportional to $1/r^2$. These terms present a nonintegrable singularity at $r = 0$ for $m = 1$, since $\hat{u}$ and $\hat{v}$ can be nonzero on the axis (13b) for $m = 1$. Using the continuity equation (9b) $\hat{u}$ and $\hat{v}$ can be expressed as

$$\frac{3\mathrm{i}m}{r^2}\hat{u} = -\frac{3\mathrm{i}m}{r}\partial_r\hat{u} + \frac{3m^2}{r^2}\hat{v} - \frac{3\mathrm{i}m}{r}\partial_z\hat{w}, \tag{C1a}$$

$$-\frac{3\mathrm{i}m}{r^2}\hat{v} = \frac{3}{r}\partial_r\hat{u} + \frac{3}{r^2}\hat{u} + \frac{3}{r}\partial_z\hat{w}, \tag{C1b}$$

as suggested by Gelfgat *et al.* [93]. Inserting these expressions into the singular terms leads to

$$-\frac{m^2+2}{r^2}\hat{u} - \frac{3\mathrm{i}m}{r^2}\hat{v} \overset{\nabla\cdot\boldsymbol{u}'=0}{=} \frac{1-m^2}{r^2}\hat{u} + \frac{3}{r}\partial_r\hat{u} + \frac{3}{r}\partial_z\hat{w}, \tag{C2a}$$

$$-\frac{2m^2+1}{r^2}\hat{v} + \frac{3\mathrm{i}m}{r^2}\hat{u} \overset{\nabla\cdot\boldsymbol{u}'=0}{=} \frac{m^2-1}{r^2}\hat{v} - \frac{3\mathrm{i}m}{r}\partial_r\hat{u} - \frac{3\mathrm{i}m}{r}\partial_z w. \tag{C2b}$$

Notice that on the right-hand sides, the terms proportional to $1/r^2$ vanish when $m = 1$. Thus, the right-hand sides of Eqs. (C2a) and (C2b) are employed for $m = 1$. Otherwise, the left-hand sides are used.

APPENDIX D: UNSTABLE MARANGONI ROLLS AT A CONTACT ANGLE $\alpha = 5°$

Marangoni cells can exist for a local Marangoni number $\mathrm{Ma}_{\mathrm{loc}} > \mathrm{Ma}_H^{\mathrm{SN}} = 82.16$. Since $\mathrm{Ma}_{\mathrm{loc}}$ decays with r, the driving is supercritical in the near-axis region with radius r^* given by $\mathrm{Ma}_{\mathrm{loc}}(r = r^*) = \mathrm{Ma}_H^{\mathrm{SN}}$. The locally varying Marangoni number provides a spatial ramp of the driving force. For ramped systems it is well known that a weak ramp from sub- to supercritical conditions significantly reduces the band of wave numbers (here the radial wave number) realizable in the supercritical region (for the Taylor-Couette system see Ref. [94]). In the extreme case, the wave number becomes unique [95].

If the variation of the local driving has a finite slope, as $\mathrm{Ma}_{\mathrm{loc}}(r)$ does in the present case, then the ramp has a certain phase pinning effect associated with the radial location r^* [96,97]. However, an even stronger phase pinning is associated with the axisymmetry of the flow which requires $u(r = 0) = 0$. This condition does not, however, determine the flow direction on the axis. Since the region of supercritical conditions expands radially as Ma_H is increased, both pinning conditions and the restricted wave number band are not in general compatible, leading to frustrated Marangoni cells. This seems to apply to the lower branch of the solution emerging from the saddle node. The situation is remedied by the amplitude of the Marangoni cells on the lower branch becoming approximately zero at values of Ma_H at which this incompatibility is strongest. As a result, the position of the radial nodal points ($u_0 \approx 0$) of the Marangoni cells remains approximately constant upon an increase of Ma_H (dominance of the pinning at the axis $r = 0$), while the amplitude of the rolls [measured by $w_0(0, \Gamma/2)$ in Fig. 8] oscillates between positive and negative values such that the flow direction of the Marangoni rolls on the axis changes almost periodically with Ma_H. The oscillations of the amplitude of the lower-branch Marangoni cells with Ma_H along the lower disconnected and the connected branches are illustrated in Fig. 36 by streamlines of the lower-branch Marangoni rolls. To eliminate the weak perturbing global thermocapillary circulation in the figure, the streamlines of the difference of the flow fields on the connected and the disconnected lower-branch solutions $\pm(\psi_0^{\mathrm{con}} - \psi_0^{\mathrm{discon}})$ are shown in Fig. 36. The sign is selected such that the flow with the lower

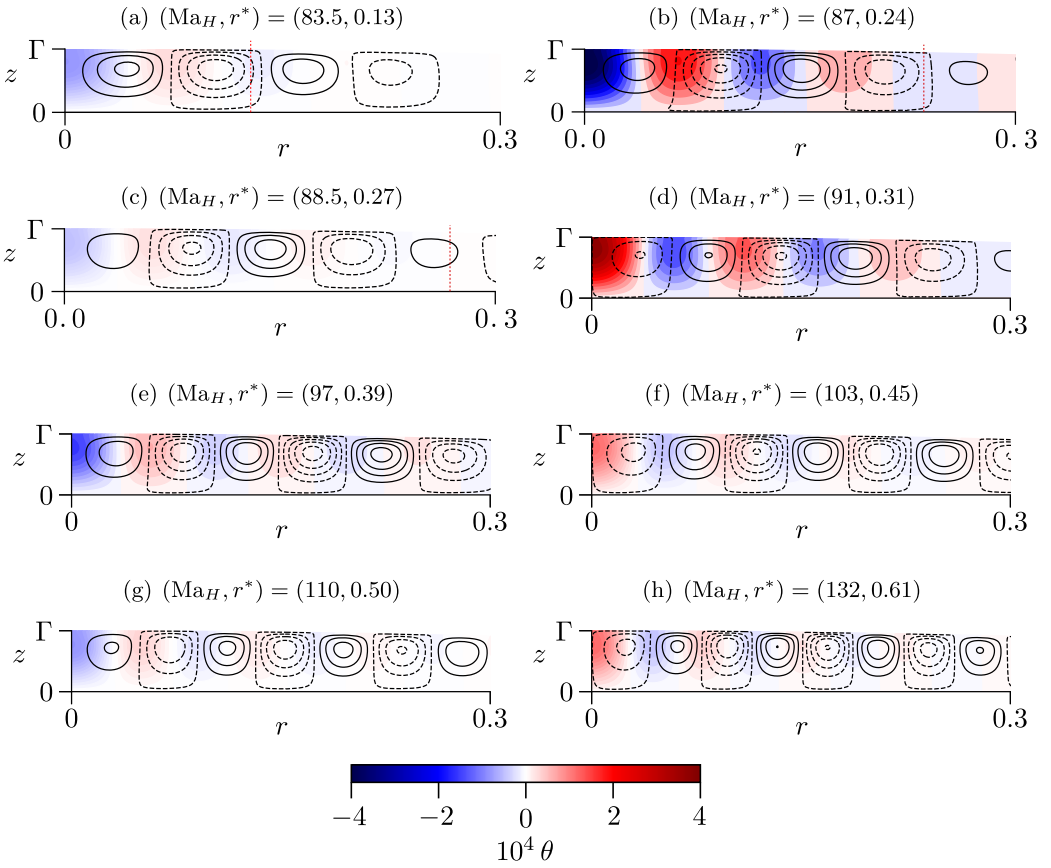

FIG. 36. Difference between the flow fields on the unstable connected and disconnected solution branches (orange and blue dotted lines in Fig. 8) evaluated at the Marangoni numbers indicated by the blue, orange and black dots in Fig. 8. Shown are streamlines and temperature fields (color). The dashed vertical red line in panels (a)–(c) indicates $r = r^*$ (see text).

velocity on the axis is subtracted from the other one. It can be noticed that the amplitude oscillates as Ma_H and r^* increase. The wave number increases slightly with Ma_H because it is determined by the local height $h(r^*)$ which decreases as Ma_H and r^* grow. The upper-branch solution (solid blue line in Fig. 8) does not exhibit these oscillations, probably because the amplitude of the Marangoni rolls is too strong.

[1] F. Giorgiutti-Dauphiné, N. Sugawara-Beda, and L. Pauchard, *Spreading and Drying of Drops and Art*, Vol. 14 of Ref. [98], Chap. 12, pp. 215–230 (2022).

[2] M. Dietzel, S. Haferl, Y. Ventikos, and D. Poulikakos, Marangoni and variable viscosity phenomena in picoliter size solder droplet deposition, ASME J. Heat Transfer **125**, 365 (2003).

[3] M. Jermy, C. Knock, S. Michielsen, F. Smith, R. Rough, T. de Castro, L. Dicken, and D. Brutin, *Drying Processes in the Formation of Bloodstains at Crime Scenes*, Vol. 14 of Ref. [98], Chap. 10 (2022).

[4] N. Laan, F. Smith, C. Nicloux, and D. Brutin, Morphology of drying blood pools, Forensic Sci. Int. **267**, 104 (2016).

[5] A. Rasheed, S. Sharma, P. Kabi, A. Saha, S. Chaudhuri, and S. Basu, Precipitation dynamics of surrogate respiratory sessile droplets leading to possible fomites, J. Colloid Interf. Sci. **600**, 1 (2021).
[6] D. Lohse, Fundamental fluid dynamics challenges in inkjet printing, Annu. Rev. Fluid Mech. **54**, 349 (2022).
[7] J. Park and J. Moon, Control of colloidal particle deposit patterns within picoliter droplets ejected by ink-jet printing, Langmuir **22**, 3506 (2006).
[8] H. Lian, L. Qi, J. Luo, R. Zhang, and K. Hu, Uniform droplet printing of graphene micro-rings based on multiple droplets overwriting and coffee-ring effect, Appl. Surf. Sci. **499**, 143826 (2020).
[9] J. Sun, Y. Sun, H. Jia, H. Bi, L. Chen, M. Que, Y. Xiong, L. Han, and L. Sun, A novel pre-deposition assisted strategy for inkjet printing graphene-based flexible pressure sensor with enhanced performance, Carbon **196**, 85 (2022).
[10] D. Brutin, B. Sobac, B. Loquet, and J. Sampol, Pattern formation in drying drops of blood, J. Fluid Mech. **667**, 85 (2011).
[11] R. Guha, F. Mohajerani, A. Mukhopadhyay, M. D. Collins, A. Sen, and D. Velegol, Modulation of spatiotemporal particle patterning in evaporating droplets: Applications to diagnostics and materials science, ACS Appl. Mater. Interfaces **9**, 43352 (2017).
[12] Y. Li, Z. Zhao, M. L. Lam, W. Liu, P. P. Yeung, C.-C. Chieng, and T.-H. Chen, Hybridization-induced suppression of coffee ring effect for nucleic acid detection, Sens. Actuators B: Chem. **206**, 56 (2015).
[13] K. Sefiane, On the formation of regular patterns from drying droplets and their potential use for bio-medical applications, J. Bionic Eng. **7**, S82 (2010).
[14] R. D. Deegan, O. Bakajin, T. F. Dupont, G. Huber, S. R. Nagel, and T. A. Witten, Capillary flow as the cause of ring stains from dried liquid drops, Nature (London) **389**, 827 (1997).
[15] R. G. Larson, Twenty years of drying droplets, Nature (London) **550**, 466 (2017).
[16] S. K. Wilson and H.-M. D'Ambrosio, Evaporation of sessile droplets, Annu. Rev. Fluid Mech. **55**, 481 (2023).
[17] D. Zang, S. Tarafdar, Y. Y. Tarasevich, M. D. Choudhury, and T. Dutta, Evaporation of a droplet: From physics to applications, Phys. Rep. **804**, 1 (2019).
[18] J. R. A. Pearson, On convection cells induced by surface tension, J. Fluid Mech. **4**, 489 (1958).
[19] M. K. Smith and S. H. Davis, Instabilities of dynamic thermocapillary liquid layers. Part 1. Convective instabilities, J. Fluid Mech. **132**, 119 (1983).
[20] K. Sefiane, A. Steinchen, and R. Moffat, On hydrothermal waves observed during evaporation of sessile droplets, Coll. Surf.A: Physicochem. Eng. Aspects **365**, 95 (2010).
[21] J.-L. Zhu and W.-Y. Shi, Longitudinal roll patterns of Marangoni instability in an easily volatile sessile droplet evaporating at constant contact angle mode, Int. J. Heat Mass Transf. **134**, 1283 (2019).
[22] J.-L. Zhu and W.-Y. Shi, Hydrothermal waves in sessile droplets evaporating at a constant contact angle mode, Int. J. Heat Mass Transf. **172**, 121131 (2021).
[23] A. Edwards, P. Atkinson, C. Cheung, H. Liang, D. Fairhurst, and F. Ouali, Density-driven flows in evaporating binary liquid droplets, Phys. Rev. Lett. **121**, 184501 (2018).
[24] Y. Li, C. Diddens, P. Lv, H. Wijshoff, M. Versluis, and D. Lohse, Gravitational effect in evaporating binary microdroplets, Phys. Rev. Lett. **122**, 114501 (2019).
[25] S. Masoudi and H. C. Kuhlmann, Axisymmetric buoyant-thermocapillary flow in sessile and hanging droplets, J. Fluid Mech. **826**, 1066 (2017).
[26] T. Takakusagi and I. Ueno, Flow patterns induced by the thermocapillary effect and resultant structures of suspended particles in a hanging droplet, Langmuir **33**, 13197 (2017).
[27] N. Riahi, Thermocapillary instability of an infinite Prandtl number fluid with negligible gravitational effects, Acta Mech. **64**, 155 (1986).
[28] M. K. Smith, Instability mechanisms in dynamic thermocapillary liquid layers, Phys. Fluids **29**, 3182 (1986).
[29] M. Wanschura, V. S. Shevtsova, H. C. Kuhlmann, and H. J. Rath, Convective instability mechanisms in thermocapillary liquid bridges, Phys. Fluids **7**, 912 (1995).
[30] H. Kuhlmann, and S. Albensoeder, Three-dimensional flow instabilities in a thermocapillary-driven cavity, Phys. Rev. E **77**, 036303 (2008).

[31] N. Garnier, and A. Chiffaudel, Two-dimensional hydrothermal waves in an extended cylindrical vessel, Eur. Phys. J. B **19**, 87 (2001).
[32] N. Imaishi, M. K. Ermakov, and W. Y. Shi, Effects of Pr and pool curvature on thermocapillary flow instabilities in annular pool, Int. J. Heat Mass Transf. **149**, 119103 (2020).
[33] D. Schwabe, A. Zebib, and B.-C. Sim, Oscillatory thermocapillary convection in open cylindrical annuli. Part 1. Experiments under microgravity, J. Fluid Mech. **491**, 239 (2003).
[34] I. Ueno, T. Kurosawa, and H. Kawamura, Thermocapillary convection in thin liquid layer with temperature gradient inclined to free surface, in *Proceedings of the 12th International Heat Transfer Conference* (Elsevier, Amsterdam, 2002), pp. 129–133.
[35] W.-Y. Shi, K.-Y. Tang, J.-N. Ma, Y.-W. Jia, H.-M. Li, and L. Feng, Marangoni convection instability in a sessile droplet with low volatility on heated substrate, Int. J. Therm. Sci. **117**, 274 (2017).
[36] T. Watanabe, T. Takakusagi, I. Ueno, H. Kawamura, K. Nishino, M. Ohnishi, M. Sakurai, and S. Matsumoto, Terrestrial and microgravity experiments on onset of oscillatory thermocapillary-driven convection in hanging droplets, Int. J. Heat Mass Transf. **123**, 945 (2018).
[37] C. Diddens, Y. Li, and D. Lohse, Competing Marangoni and Rayleigh convection in evaporating binary droplets, J. Fluid Mech. **914**, A23 (2021).
[38] F. Carle, B. Sobac, and D. Brutin, Hydrothermal waves on ethanol droplets evaporating under terrestrial and reduced gravity levels, J. Fluid Mech. **712**, 614 (2012).
[39] G. Karapetsas, O. K. Matar, P. Valluri, and K. Sefiane, Convective rolls and hydrothermal waves in evaporating sessile drops, Langmuir **28**, 11433 (2012).
[40] V. G. Levich, *Physicochemical Hydrodynamics* (Prentice-Hall, Hoboken, NJ, 1962).
[41] F. Romanò and H. C. Kuhlmann, Heat transfer across the free surface of a thermocapillary liquid bridge, Tech. Mech.- Eur. J. Eng. Mech. **39**, 72 (2019).
[42] M. Stojanovic and H. C. Kuhlmann, Stability of thermocapillary flow in high-Prandtl-number liquid bridges exposed to a coaxial gas stream, Microgravity Sci. Technol. **32**, 953 (2020).
[43] W. Schneider, Surfaces as nonautonomous thermodynamic systems, in M. Pilotelli and G. P. Beretta, eds., *Proceedings of the 12th Joint European Thermodynamics Conference* (Snoopy, Brescia, Italy, 2013), pp. 178–185.
[44] M. F. Schatz and G. P. Neitzel, Experiments on thermocapillary instabilities, Annu. Rev. Fluid Mech. **33**, 93 (2001).
[45] P.-E. des Boscs and H. C. Kuhlmann, Stability of obliquely driven cavity flow, J. Fluid Mech. **928**, A25 (2021).
[46] J. Nitsche, Über ein Variationsprinzip zur Lösung von Dirichlet-Problemen bei Verwendung von Teilräumen, die keinen Randbedingungen unterworfen sind, Abh. Math. Semin. Univ. Hambg. **36**, 9 (1971).
[47] A. Y. Gelfgat, P. Z. Bar-Joseph, and A. L. Yarin, Stability of multiple steady states of convection in laterally heated cavities, J. Fluid Mech. **388**, 315 (1999).
[48] M. Alnaes, J. Blechta, J. Hake, A. Johansson, B. Kehlet, A. Logg, C. Richardson, J. Ring, M. E. Rognes, and G. N. Wells, The FEniCS project version 1.5, Arch. Num. Softw. **3**, 9 (2015).
[49] P. Virtanen, R. Gommers, T. E. Oliphant, M. Haberland, T. Reddy, D. Cournapeau, E. Burovski, P. Peterson, W. Weckesser, J. Bright, S. J. van der Walt, M. Brett, J. Wilson, K. J. Millman, N. Mayorov, A. R. J. Nelson, E. Jones, R. Kern, E. Larson, C. J. Carey, İ. Polat, Y. Feng, P. van Mulbregt, and SciPy 1.0 Contributors, SciPy 1.0: Fundamental algorithms for scientific computing in Python, Nat. Methods **17**, 261 (2020).
[50] R. B. Lehoucq, D. C. Sorensen, and C. Yang, *ARPACK Users' Guide: Solution of Large-Scale Eigenvalue Problems with Implicitly Restarted Arnoldi Methods* (SIAM, Philadelphia, PA, 1998).
[51] P.-E. des Boscs (private communication) (2019).
[52] K. Meerbergen, A. Spence, and D. Roose, Shift-invert and Cayley transforms for detection of eigenvalues with largest real part of nonsymmetric matrices, BIT **34**, 409 (1994).
[53] M. Stojanovic, F. Romanò, and H. C. Kuhlmann, Stability of thermocapillary flow in liquid bridges fully coupled to the gas phase, J. Fluid Mech. **949**, A5 (2022).
[54] Q. Wang, X. Zhang, Y. Zhang, and Q. Yi, AUGEM: Automatically generate high-performance dense linear algebra kernels on x86 CPUs, in *Proceedings of the International Conference for High Performance*

Computing, Networking, Storage and Analysis (SC'13), edited by W. Gropp and S. Matsuoka (ACM, New York, NY, 2014), p. 25.
[55] D. E. Muller, A method for solving algebraic equations using an automatic computer, Math. Tables Other Aids Comput. **10**, 208 (1956).
[56] C. Nienhüser and H. C. Kuhlmann, Stability of thermocapillary flows in non-cylindrical liquid bridges, J. Fluid Mech. **458**, 35 (2002).
[57] S. Rosenblat, G. M. Homsy, and S. H. Davis, Nonlinear Marangoni convection in bounded layers. Part 1. Circular cylindrical containers, J. Fluid Mech. **120**, 91 (1982).
[58] M. F. Schatz, S. J. VanHook, W. D. McCormick, J. B. Swift, and H. L. Swinney, Onset of surface-tension-driven Bénard convection, Phys. Rev. Lett. **75**, 1938 (1995).
[59] E. L. Koschmieder and S. A. Prahl, Surface-tension-driven Bénard convection in small containers, J. Fluid Mech. **215**, 571 (1990).
[60] N. Imaishi, S. Yasuhiro, Y. Akiyama, and S. Yoda, Numerical simulation of oscillatory Marangoni flow in half-zone liquid bridge of low Prandtl number fluid, J. Cryst. Growth **230**, 164 (2001).
[61] J. Leypoldt, H. C. Kuhlmann, and H. J. Rath, Three-dimensional numerical simulation of thermocapillary flows in cylindrical liquid bridges, J. Fluid Mech. **414**, 285 (2000).
[62] H. Kuhlmann and U. Schoisswohl, Flow instabilities in thermocapillary-buoyant liquid pools, J. Fluid Mech. **644**, 509 (2010).
[63] Y.-R. Li, X.-J. Quan, L. Peng, N. Imaishi, S.-Y. Wu, and D.-L. Zeng, Three-dimensional thermocapillary-buoyancy flow in a shallow molten silicon pool with Cz configuration, Int. J. Heat Mass Transf. **48**, 1952 (2005).
[64] S. H. Davis and G. M. Homsy, Energy stability theory for free-surface problems: Buoyancy-thermocapillary layers, J. Fluid Mech. **98**, 527 (1980).
[65] F. Gallaire and P.-T. Brun, Fluid dynamic instabilities: Theory and application to pattern forming in complex media, Phil. Trans. R. Soc. A. **375**, 20160155 (2017).
[66] H. C. Kuhlmann and F. Romanò, *The Lid-Driven Cavity*, Vol. 50 of *Computational Methods in Applied Sciences* (Springer, Berlin, 2018), pp. 233–309.
[67] M. Levenstam, and G. Amberg, Hydrodynamic instabilities of thermocapillary flow in a half-zone, J. Fluid Mech. **297**, 357 (1995).
[68] S. E. Widnall and C.-Y. Tsai, The instability of the thin vortex ring of constant vorticity, Philos. Trans. R. Soc. Lond. A **287**, 273 (1977).
[69] S. Albensoeder and H. C. Kuhlmann, Three-dimensional instability of two counter-rotating vortices in a rectangular cavity driven by parallel wall motion, Eur. J. Mech. B Fluids **21**, 307 (2002).
[70] S. Albensoeder and H. C. Kuhlmann, Linear stability of rectangular cavity flows driven by anti-parallel motion of two facing walls, J. Fluid Mech. **458**, 153 (2002).
[71] B. J. Bayly, Three-dimensional instability of elliptical flow, Phys. Rev. Lett. **57**, 2160 (1986).
[72] R. T. Pierrehumbert, Universal short-wave instability of two-dimensional eddies in an inviscid fluid, Phys. Rev. Lett. **57**, 2157 (1986).
[73] H. C. Kuhlmann and H. J. Rath, Hydrodynamic instabilities in cylindrical thermocapillary liquid bridges, J. Fluid Mech. **247**, 247 (1993).
[74] K. Khoshmanesh, S.-Y. Tang, J. Y. Zhu, S. Schaefer, A. Mitchell, K. Kalantar-Zadeh, and D. Dickey, Liquid metal enabled microfluidics, Lab Chip **17**, 974 (2017).
[75] G. H. Perry and N. K. Roberts, Surface tension of mercury between 15 and 50°C by the sessile drop method, J. Chem. Eng. Data **26**, 266 (1981).
[76] V. Y. Prokhorenko, V. V. Roshchupkin, M. A. Pokrasin, S. V. Prokhorenko, and V. V. Kotov, Liquid gallium: Potential uses as a heat-transfer agent, High Temp. **38**, 954 (2000).
[77] F. Romanò and H. C. Kuhlmann, Finite-size coherent structures in thermocapillary liquid bridges, Int. J. Micrograv. Sci. Appl. **36**, 360201 (2019).
[78] P. Dell'Aversana, V. Tontodonato, and L. Carotenuto, Suppression of coalescence and of wetting: The shape of the interstitial film, Phys. Fluids **9**, 2475 (1997).
[79] G. P. Neitzel and P. Dell'Aversana, Noncoalescence and nonwetting behavior of liquids, Annu. Rev. Fluid Mech. **34**, 267 (2002).

[80] S. Kumar, M. Medale, and D. Brutin, Numerical model for sessile drop evaporation on heated substrate under microgravity, Int. J. Heat Mass Transf. **195**, 123150 (2022).
[81] C. Diddens, H. Tan, L. Pengyu, M. Versluis, J. G. M. Kuerten, X. Zhang, and D. Lohse, Evaporating pure, binary and ternary droplets: Thermal effects and axial symmetry breaking, J. Fluid Mech. **823**, 470 (2017).
[82] Y. Li, P. Lv, C. Diddens, and D. Lohse, Physicochemical hydrodynamics of the phase segregation in an evaporating binary microdroplet, J. Fluid Mech. **946**, A37 (2022).
[83] L. Y. Barash, T. P. Bigioni, V. M. Vinokur, and L. N. Shchur, Evaporation and fluid dynamics of a sessile drop of capillary size, Phys. Rev. E **79**, 046301 (2009).
[84] A. A. Gavrilina and L. Y. Barash, Modeling unsteady Bénard-Marangoni instabilities in drying volatile droplets on a heated substrate, J. Exp. Theor. Phys. **132**, 302 (2021).
[85] D. Hu and H. Wu, Numerical study and predictions of evolution behaviors of evaporating pinned droplets based on a comprehensive model, Int. J. Therm. Sci. **96**, 149 (2015).
[86] S. Semenov, V. M. Starov, R. Rubio, and M. G. Velarde, Instantaneous distribution of fluxes in the course of evaporation of sessile liquid droplets: Computer simulations, Colloids Surf. A Physicochem. Eng. Asp. **372**, 127 (2010).
[87] H. V. Tran, T. A. H. Nguyen, S. R. Biggs, and A. V. Nguyen, On the predictions for diffusion-driven evaporation of sessile droplets with interface cooling, Chem. Eng. Sci. **177**, 417 (2018).
[88] J.-L. Zhu, L. Feng, and W.-Y. Shi, Influence of thermal properties on hydrothermal waves in evaporating sessile droplets, Phys. Fluids **33**, 102107 (2021).
[89] E. Yim, A. Bouillant, and F. Gallaire, Buoyancy-driven convection of droplets on hot nonwetting surfaces, Phys. Rev. E **103**, 053105 (2021).
[90] K. Yang, F. Hong, and P. Cheng, A fully coupled numerical simulation of sessile droplet evaporation using arbitrary Lagrangian-Eulerian formulation, Int. J. Heat Mass Transf. **70**, 409 (2014).
[91] L. Y. Barash, Dependence of fluid flows in an evaporating sessile droplet on the characteristics of the substrate, Int. J. Heat Mass Transf. **84**, 419 (2015).
[92] X. Chen, X. Wang, P. G. Chen, and Q. Liu, Thermal effects of substrate on Marangoni flow in droplet evaporation: Response surface and sensitivity analysis, Int. J. Heat Mass Transf. **113**, 354 (2017).
[93] A. Y. Gelfgat, P. Z. Bar-Yoseph, A. Solan, and T. A. Kowalewski, An axisymmetry-breaking instability of axially symmetric natural convection, Int. J. Trans. Phenomena **1**, 173 (1999).
[94] G. Ahlers, D. S. Cannell, M. A. Dominguez-Lerma, and R. Heinrichs, Wave number selection and Eckhaus instability in Couette-Taylor flow, Physica D **23**, 202 (1986).
[95] H. Riecke and H.-G. Paap, Perfect wave-number selection and drifting patterns in ramped Taylor vortex flow, Phys. Rev. Lett. **59**, 2570 (1987).
[96] M. Lücke and D. Roth, Structure and dynamics of Taylor vortex flow and the effect of subcritical driving ramps, Z. Phys. B **78**, 147 (1990).
[97] H. Riecke, Pattern selection by weakly pinning ramps, Europhys. Lett. **2**, 1 (1986).
[98] D. Brutin and K. Sefiane, eds., *Drying of Complex Fluid Drops: Fundamentals and Applications*, Vol. 14 of *Soft Matter Series* (Royal Society of Chemistry, London, UK, 2022).